

A High Incidence of Central Star Formation Inferred from Color Gradients of Galaxies at $z > 4$

BINGCHENG JIN (金秉诚) ^{1,2} LUIS C. HO ^{1,2} AND WEN SUN (孙文) ^{1,2}

¹*Kavli Institute for Astronomy and Astrophysics, Peking University, Beijing 100871, China*

²*Department of Astronomy, School of Physics, Peking University, Beijing 100871, China*

ABSTRACT

We present a study of the galaxy color gradient at $4 < z < 8$, using the high-resolution imaging data from the JWST Cosmic Evolution Early Release Science (CEERS) program. We use `GalfitM` to fit the light profile of 669 galaxies simultaneously for better characterization of wavelength dependency of structural parameters. We apply the parametric methodology of quantifying color gradient out to $z > 4$, finding a neutral distribution of the effective radius and Sérsic index variation. This implies a weak dependency of structural parameters on wavelength at high redshift, consistent with the latest JWST results. Using the three color gradient proxies, we find that the color gradient has a pronounced dependency on its sizes, masses, and rest-frame color: positive color gradients tend to inhabit galaxies with smaller sizes, smaller stellar mass, and bluer SEDs. By studying the potential influence of AGNs, we claim that stellar emission is the major driver of the central blue excess, which leads to a high incidence of central star formation perceived in the high- z Universe.

Keywords: Early universe (435); Galaxy formation (595); Galaxy evolution (594); High-redshift galaxies (734)

1. INTRODUCTION

The structure and morphology of galaxies, and how these properties evolve with time, encode important clues about galaxy formation and evolution. Over the past few decades, theoretical and observational studies have proposed many of the mechanisms that drive the morphological evolution of galaxies. The Monolithic Collapse model (Eggen et al. 1962) suggests that galaxies form in a single rapid collapse, and the subsequent star formation can explain the build-up of classical bulges and elliptical galaxies. The Hierarchical model (White & Frenk 1991; Steinmetz & Navarro 2002) predicts that the galaxy structure reflects the varied accretion histories, based on the bottom-up paradigm of cold dark matter halo (e.g., Wang et al. 2011). The process can emphasize the role of accretion and merging, which contributes to the growth of galaxy disks and the formation of early-type systems. While these two models are often challenged by modern observations (e.g., Forbes & Bridges 2010; Kormendy et al. 2010), a new scheme

called the “inside-out growth” (van Dokkum et al. 2010; Pérez et al. 2013; Marian et al. 2018; Frankel et al. 2019) is proposed, which incorporate the advantages of both models. In this scenario, the galaxy grows from the early build up of the central bulge, followed by the gradual growth of the disk driven by accretion and minor mergers. The inside-out growth scenario is supported by the observation from different perspectives, including tracing coherent star formation (Nelson et al. 2016; Matharu et al. 2024) and inside-out quenching (Tacchella et al. 2015; Abdurro’uf & Akiyama 2018), and comparing size evolution along cosmic time (Suess et al. 2019; van der Wel et al. 2024). Among them, the color gradient, namely the radial variation of color, can be the most simple and direct way to examine the case.

Observational evidence of color gradient has been comprehensively established in many studies concerning our local Universe (Muñoz-Mateos et al. 2007; Kelvin et al. 2012; Gong et al. 2023). Kennedy et al. (2015) declared ubiquitous negative color gradients (i.e., redder center and bluer outskirts) in the galaxy database of Driver et al. (2018), and a stronger negative color gradient for late-type galaxies, or systems with smaller Sérsic indices.

Galaxies out to $z = 1 - 2$ can establish such negative color gradients as well (Miller et al. 2023), but weaker trend and larger scatter towards higher redshift are also perceived (Suess et al. 2019; van der Wel et al. 2024). A negative color gradient implies a negative gradient in mass-to-light ratio (van der Wel et al. 2024), making the stellar mass profile more concentrated than the given light profile. Galaxies with negative color gradient show smaller half-mass radii than half-light radii, and van der Wel et al. (2024) found that the ratio between the half-mass radius and half-light radius is increasing with redshift, from 0.7 at $z \approx 1$ to almost unity at $z \approx 2.5$. The evolution pattern that negative color gradients generally get enhanced from the early Universe to the present day, is suggestive of the inside-out growth scenario.

Metallicity gradient, age gradient, and their interplay are widely believed to be the contributing factors to the spatial color variation. Early-type galaxies are more influenced by their metal-rich centers (Vader et al. 1988; Marian et al. 2018), while late-type galaxies are expected to possess prominent negative color gradient for their younger stellar population in the outer region (Ryder & Dopita 1994).

Dust attenuation (Calzetti et al. 2000; Salim & Narayanan 2020) can also account for the spatial variation of color, e.g., the centrally concentrated dust can redden the inner region, providing an alternative explanation rather than inside-out growth (Graham & Worley 2008; Miller et al. 2022; Zhang et al. 2023). Wang et al. (2017) found that when taking into account the radial A_V profile, the sSFR gradient is almost flat except for galaxies with $M_\star \gtrsim 10^{10.5} M_\odot$. Nedkova et al. (2024b) use VELA simulations (Ceverino et al. 2014) to show that the dust attenuation alone should suffice to explain the size discrepancy between rest-frame ultraviolet (UV) and optical (Mosleh et al. 2012).

The role of dust attenuation is still under debate, especially for the high- z Universe. Though the spatial distribution of dust can provide an alternative way other than that of the stellar population to explain the color gradient, in the general case the effect of dust attenuation is found to be less significant at $z \gtrsim 4$ (e.g., Fudamoto et al. 2020; Looser et al. 2024; Mitsuhashi et al. 2024), as metal enrichment is barely proceeded and lower dust-to-gas ratio is expected especially for low-mass systems (Li et al. 2019).

The James Webb Space Telescope (JWST) enables us to resolve galaxies that are fainter, redder, and at higher redshifts, especially in their rest-frame optical and near-infrared (e.g., Abdurro'uf et al. 2023; Giménez-Arteaga et al. 2023; Matharu et al. 2023). No trends between morphology and colors are detected at $z = 7 - 12$ with

JWST-GLASS (Yang et al. 2022; Treu et al. 2023). Ono et al. (2024) also found that the ratio of the effective radius in rest-frame UV and optical are almost congruent at $z > 4$, and even a larger fraction of positive color gradient was declared at the same time (Morishita et al. 2024). While on the other hand, JWST has discerned negative color gradients already in place at high redshift regime: Ji et al. (2024) used JADES (JWST Advanced Deep Extragalactic Survey; Eisenstein et al. 2024) survey to study the size evolution of galaxies at $0.5 < z < 5$, and they found evidence for negative color gradient for massive quiescent systems at $z > 3$; Baker et al. (2024) also reported a core-disk galaxy at spectroscopic redshift $z = 7.43$, which indicates a very early establishment of inside-out growth.

Those seemingly contradictory results call for a more exhaustive study of the color gradient at high redshift. It is still unclear whether the color gradient still exists at high redshift, and if so, under what conditions the color gradient can be established at such an early stage, what is the main driver behind it, whether it is correlated with other properties of galaxies, how it evolves with time, and whether it is like what is expected in the inside-out growth scenario.

In this work, we aim to study the color gradient of galaxies at $z > 4$, seeking the dependency of color gradient on galaxy properties. We use NIRCcam imaging data from the Cosmic Evolution Early Release Science (CEERS; Finkelstein et al. 2023) Survey, which already has a rich set of multi-wavelength data offered by overlapping parallel observations. Although broadly similar topics have been studied recently with data from JWST, as mentioned above, our approach differs in several key aspects. It is a difficult challenge to measure structural parameters precisely with robust uncertainties for high-redshift galaxies, even with impressive data from JWST. In our study, the contribution of observational effects is included in the final error budget. Under what conditions can we quantify color gradients robustly are carefully examined. Since the variation of structural parameters with wavelength is our focus, we opt to use GalfitM (Häußler et al. 2013; Vika et al. 2013) for a more robust and accurate measurement of the light distribution between bands simultaneously. We quantify color gradients with three different color gradient proxies and study their dependencies on galaxy properties of different aspects. By doing so, we expect to establish a more complete picture of color gradient evolution since the epoch of reionization.

The paper is organized as follows. Section 2 describes the observation data we use and how we extract high- z sources based on the published catalog. Section 3 intro-

duces how we measure the structural parameters and band flux using `GalfitM`. Section 4 illustrates our characterization of color gradient. In Section 5, we show the major results. Section 6 discusses how the results are incorporated into the current understanding, and the implications for the early stage of galaxy structural assembly. Section 7 summarizes the main findings of this work. We assume a cosmology with $H_0 = 67.7 \text{ km s}^{-1} \text{ Mpc}^{-1}$, $\Omega_m = 0.307$, and $\Omega_\Lambda = 0.693$ (Planck Collaboration et al. 2020). All magnitudes in the following sections are in the absolute bolometric (AB) system.

2. DATA ACQUISITION AND SAMPLE DEFINITION

2.1. CEERS Data

We use the NIRCcam imaging data from the Cosmic Evolution Early Release Science (CEERS) program, which covers $\sim 100 \text{ arcmin}^2$ with three short wavelength (SW) bands (F115W, F150W, F200W) and four long wavelength (LW) bands (F277W, F356W, F410M, F444W). The mosaics of 10 NIRCcam pointings overlap with the CANDELS Extended Groth Strip (EGS) field, one of the most well-studied fields in the era of Hubble Space Telescope (Koekemoer et al. 2011). The CEERS survey is designed to study the processes of galaxy assembly and the abundance and physical nature of galaxies in the early Universe.

The CEERS team has published their data release after 2 epochs of observations (Finkelstein et al. 2023), and we directly download the latest version of the reduced data from CEERS website¹. The data reduction process is discussed thoroughly in Bagley et al. (2023a), and reduction scripts are available on GitHub². Though various approaches have been adopted to reduce the data in CEERS field (e.g., Morishita et al. 2024; Zhuang et al. 2024) for each of their purposes, the measurements of structural parameters are mostly consistent with each other (see Figure 9 in Sun et al. 2024 for example).

2.2. Point-spread Function

The point-spread function (PSF) is crucial in determining structural parameters, especially for small high- z galaxies. We choose to construct the PSF model for each band by stacking isolated, unsaturated point-like sources in the field for more stable performance in real observation (see more detailed analysis and performance tests in Section 3.2 and Appendix A of Sun et al. 2024). For the four pointings of CEERS Epoch 1 observations

(CEERS1, CEERS2, CEERS3, and CEERS6), we use the PSF model from Sun et al. (2024). For the other six pointings of CEERS Epoch 2 observations, we stack selected isolated, unsaturated point-like sources to construct a PSF for each NIRCcam filter. These point-like sources are identified from our source detection result (Section 2.3), which have full-width at half-maximum FWHM < 6 pixels, as determined by fitting a two-dimensional Gaussian profile to an image cutout of size 7 times the Kron (1980) radius of the source. Sources contaminated by neighboring sources within 81 pixels are removed.

We identify 37 point-like sources in the six pointings of CEERS Epoch 2 observations. Because of the relatively small number of objects available, we do not produce a separate PSF for each pointing. Instead, for each filter, the objects in all six pointings of CEERS Epoch 2 observations are combined to create a master, stacked PSF of high signal-to-noise ratio. PSF variations across different pointings of the same epoch should be small because they were taken close in time and utilize the same dither pattern (Bagley et al. 2023a). A 81×81 pixel cutout is extracted for each object, and all the cutouts are 4 times oversampled to align their centers after removing the background. The final PSF is constructed by mean-combining the individual stars and resampling the oversampled images to their original resolution.

2.3. Sample Definition

To prepare for the image analysis, we carry out the following steps to extract sources from the CEERS mosaics. First, we stack all long wavelength (LW) band images (F277W, F356W, F410M, F444W) weighted by their error to create a high signal-to-noise ratio image, where we perform 1σ source detection using `photutils` (Bradley et al. 2024). As many high-redshift galaxies are faint, and may be outshined by the bright neighboring sources, we use function `deblend_sources` to separate them. The catalog is then constructed with the deblended segmentation map. We crossmatch our source catalog with CANDELS photometric redshift catalog (Stefanon et al. 2017), whose detection is based on the HST F160W band, with a 5σ limiting magnitude of 27.6 mag. This study focuses on galaxies in the redshift range of $4 < z < 8$. Although other catalogs are available (e.g., Duncan et al. 2019; Whitney et al. 2021; Kodra et al. 2023), we choose Stefanon et al.’s catalog for convenience because it provides both photometric redshifts and stellar masses. Also, Stefanon et al.’s main photometry catalog includes self-consistent photometry across 22 bands, covering wavelengths from 0.4 to $8 \mu\text{m}$, which

¹ <https://ceers.github.io/releases.html>

² <https://github.com/ceers/ceers-nircam>

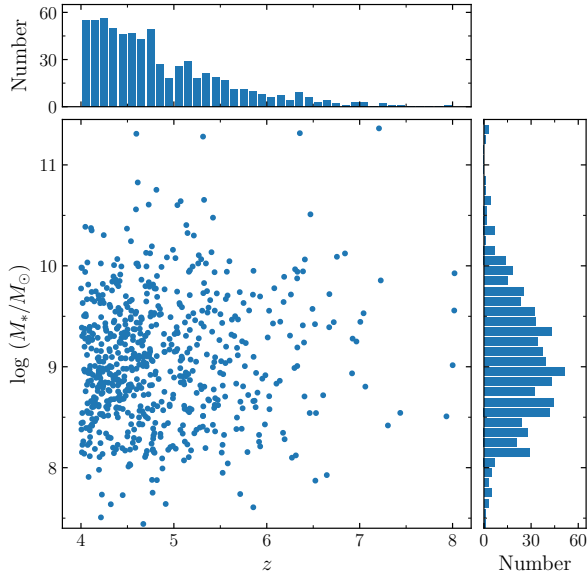


Figure 1. Distribution of redshift and stellar mass of the sample.

will benefit our analysis of rest-frame color in Section 4.2 and Section 5.3.

For sources exposed in more than one pointing, as these sources often appear on the edge of the mosaics, we exclude redundant cutouts and ensure that the survived cutout has as many available pixels as possible for either background estimation or the fitting process. The final sample includes 669 galaxies (Table A1), after removing galaxies that do not have complete imaging. The redshift and stellar mass of the sample of 669 galaxies are shown in Figure 1.

3. IMAGE ANALYSIS

3.1. Model Fitting

Galaxy light distribution can be well described by the Sérsic profile (Sérsic 1968), which is defined as

$$\mu(R) = \mu_e \exp \left\{ -b_n \left[\left(\frac{R}{R_e} \right)^{1/n} - 1 \right] \right\}, \quad (1)$$

where I_e is the surface brightness at the effective radius R_e , and b_n is a constant that depends on the Sérsic index n .

We use *GalfitM* (Häußler et al. 2013; Vika et al. 2013, 2015), to model the light distribution of galaxies. *GalfitM* is a modified version of *Galfit* (Peng et al. 2002; Peng et al. 2010) capable of fitting multi-band images with polynomial constraints on model parameters. Previous studies have shown that constraining n and R_e of the components by second-order polynomial will

improve accuracy and stability in revealing the multi-wavelength light distribution of galaxies, especially for those with low signal-to-noise ratio at some bands (Vika et al. 2013).

To generate cutouts for the following image analysis, we use 7 times the Kron radius to define the image size, because it is large enough to have as many pixels available as possible for background estimation while not slowing down the fitting process too much. We also measure the basic properties of the galaxies using *source_catalog* in non-parametric ways, including the Kron flux, axis ratio (AR), and position angle (PA), for convenience of initial guess of the model parameters.

Our image analysis method is based on Sun et al. (2024), we mask out contaminating sources in the cutout by dilating the segmentation map (see Section 2.3) with a “growth radius” (Ho et al. 2011; Huang et al. 2013), but for those contaminating sources that are adjacent to the target galaxy, we choose not to mask them out in the *GalfitM* bad pixel input, as they may have a significant impact on the light distribution of the target galaxy. Instead, we use multiple components to model the light distribution.

We estimate the local background level by excluding every detection in the cutout with dilating masks (i.e., not only the surrounding objects but also the target galaxy itself will be excluded). For the input science image, we subtract the mean value of the background pixels. For the input weight (sigma) image, we scale the error map cut from ERR extension, such that its background pixel value level equals the science image background standard deviation.

Different from previous studies including Vika et al. (2015); Sun et al. (2024), in our fit, we apply extra constraints to n and R_e of the components to ensure monotonic dependencies of these parameters on wavelength (i.e., n and R_e are constrained linearly with wavelength). Though the quadratically constrained fit allows curvature in the dependency of n and R_e on wavelength, providing more flexibility and accuracy in the fitting process, it sometimes introduces non-physical solutions, where n and R_e can have non-monotonic dependencies on wavelength. More explicitly, if a galaxy has a different spatial distribution for stellar population (e.g., a centrally concentrated red bulge with an extended bluer disk or a star-forming core with a quiescent envelope), and since the light distribution at redder bands should be more dominated by red stellar population, the measurement can only go one way from the bluer bands to the redder bands, leaving no room for up-and-down behavior for n and R_e . The same argument applies to dust attenuation because the nature of all these mecha-

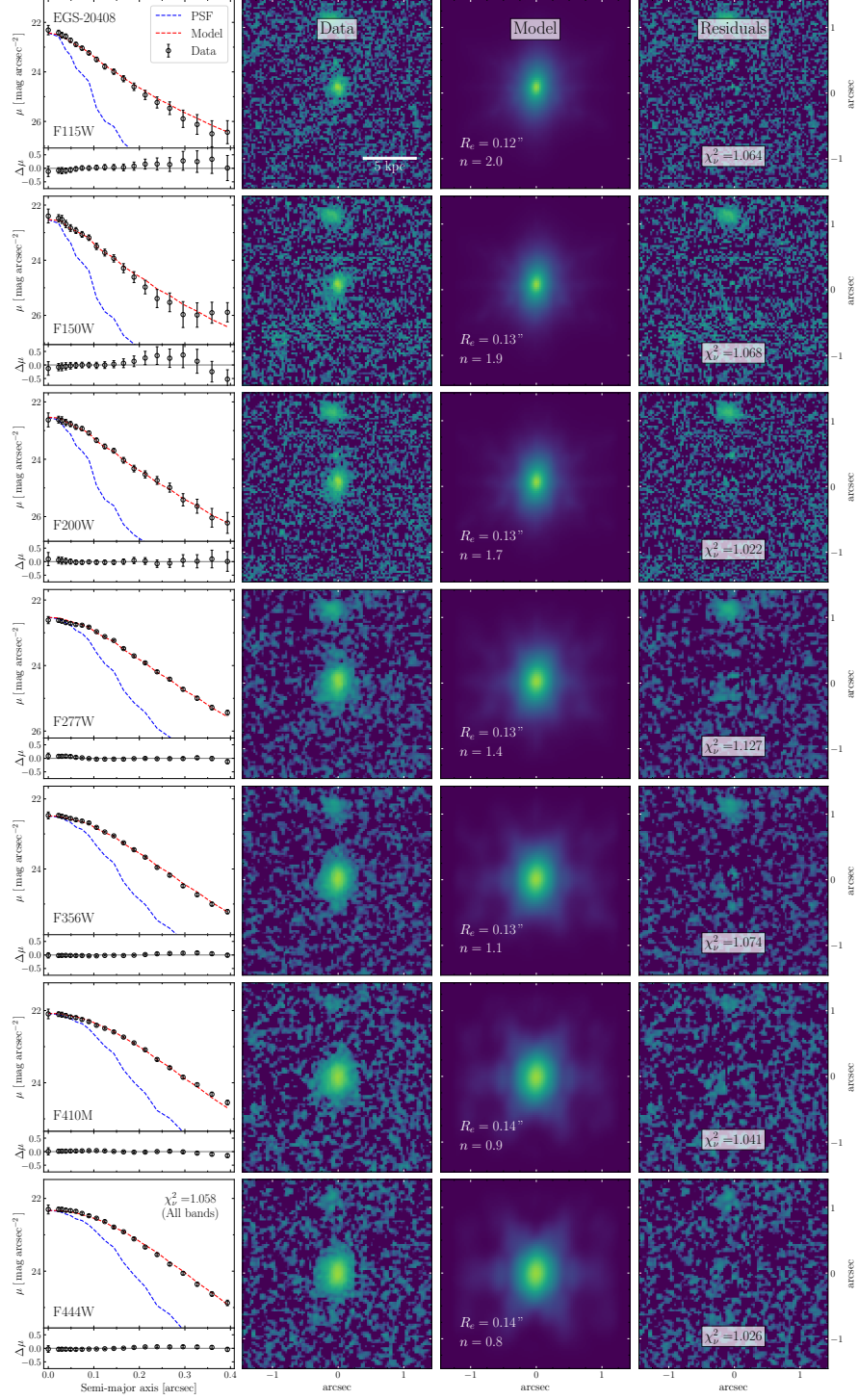


Figure 2. Simultaneous, multiband fitting of the galaxy EGS-20408 (Stefanon et al. 2017) at $z = 5.373$. Rows from top to bottom are the results for the F115W, F150W, F200W, F277W, F356W, F410M, and F444W bands. Columns from left to right are the 1D surface brightness profile, input science image, model image (convolved with the PSF), and residual image. The χ^2_ν for each band is given in the residual image, and the structural parameters are shown in the lower-left corner of the model image. In the 1D profile, the black points with error bars are measured by aperture photometry, the red dashed line shows the model profile, and the blue dashed line represents the PSF, scaled to match the model profile.

nisms is monotonically changing with wavelength (e.g., the dust attenuation is more severe at bluer bands).

The initial guess is sometimes crucial to the convergence of the fitting process. In this case, we make sure every target galaxy is placed right at the center of the cutout, and only allow their position to vary slightly from our initial guess, to compensate for the subtle offset introduced by WCS calibration. For every image, the initial guess of n is set to be 3.0, and that of R_e is based on the median value of the half-light radius measured by `photutils`. The initial guess of position angle and axis ratio are also from the measurement discussed above, and they are not allowed to vary between bands. The initial guess of magnitude is derived by Kron aperture flux in each band, and we allow magnitudes to vary freely between bands, i.e., the Chebyshev polynomials order is set to be 7 which corresponds to all 7 band images in our case.

Ono et al. (2024) reported that including blended sources without a proper mask can lead to a larger rest-frame optical-to-UV size ratio. To avoid the blendness, we visually inspect every single cutout and our segmentation map to assign a flag about the blendness as summarized in Table A1: 1) isolated; 2) blended by adjacent objects that are properly segmented; 3) heavily blended by the contaminating sources. For isolated targets (flag 1), the fitting process is straightforward, and a single Sérsic profile is sufficient to describe the light distribution. We show an example of our single Sérsic component fit in Figure 2. For flag 2, we apply additional components to the fit, as shown in Figure 3. While the multiple components fit takes much longer to converge, we set the initial guess of the extra components as the median value from `Galfit` single band fits if they are satisfying, or plug in the values by human inspection. There are 114 galaxies with flag 3. We use galaxies with blendness flags 1 and 2 in our following analysis.

3.2. Uncertainty of Structural Parameters

Similar to `Galfit`, `GalfitM` estimates the uncertainties using the curvature of the χ^2 surface around the best-fit solution. Many studies have shown that the uncertainties returned by `Galfit` or `GalfitM` are underestimated (Häußler et al. 2022; Nedkova et al. 2024a). To address this issue, our error estimation is based on mocks described in Zhuang & Ho (2022), where we generate a set of simulated images with known input parameters to resemble real observations. We first create a clean image for each galaxy with its best-fit parameters and convolve them with the PSF model. Then we mimic realistic observation by adding Poisson noise of the source and considering background noise levels that

differ from every specific image. 100 mocks are generated for each galaxy. The same `GalfitM` configuration is then applied to the mock images. By conducting the input-output experiment, we adopt the median value as the final measurement and incorporate the standard deviation into the final error budget.

Sun et al. (2024) have shown that the measurement will be biased by the cosmological effects: the magnitude of the faintest galaxy will be underestimated by 0.3 mag at $z = 4$, and the size will be underestimated especially for small galaxies. The fluctuation of measurement will be more significant for large n systems, and a large scatter is perceived at the highest redshift end. Following the mock analysis described in Appendix B of Sun et al. (2024), we correct for the bias and incorporate the fluctuation into the final error budget.

4. COLOR GRADIENT

4.1. Quantification of Color Gradient

Previous attempts to quantify color gradients include charting color profiles (Miller et al. 2023), calculating central stellar mass surface density (Ji et al. 2024). Also some notations are introduced to describe the color gradient: Vulcani et al. (2014) use \mathcal{N}, \mathcal{R} to characterize the Sérsic index and effective radius variation (the ratio of measured properties between bands); van der Wel et al. (2024) define ΔC , which basically compares the flux measured at 0.5 and 2.0 times the half-light radii between different bands. Similarly, Marian et al. (2018) use the slope of the surface color profile $\nabla_{\lambda_1-\lambda_2}(r_M, r_m)$ (at radius r_M and r_m) to quantify the color gradient.

Here we focus on the dependency of n and R_e on wavelength, as it maximizes the use of multi-wavelength information of the galaxy light distribution. We define the Sérsic index variation \mathcal{N} as:

$$\mathcal{N} = \frac{n^b}{n^r}, \quad (2)$$

where n^b and n^r denote the Sérsic index measured at a blue band (b) and a red band (r), respectively. A large n at a redder band can indicate an early-type morphology observed at longer wavelengths. This usually corresponds to a redder center region of the galaxy, and $\mathcal{N} < 1$ describes the scenario mentioned above.

We define the effective radius variation \mathcal{R} as:

$$\mathcal{R} = \frac{R_e^b}{R_e^r}, \quad (3)$$

where R_e^b and R_e^r denote the effective radius measured at a blue band and a red band, respectively. A larger R_e at a bluer band can indicate a more extended structure perceived at shorter wavelengths. This usually corresponds

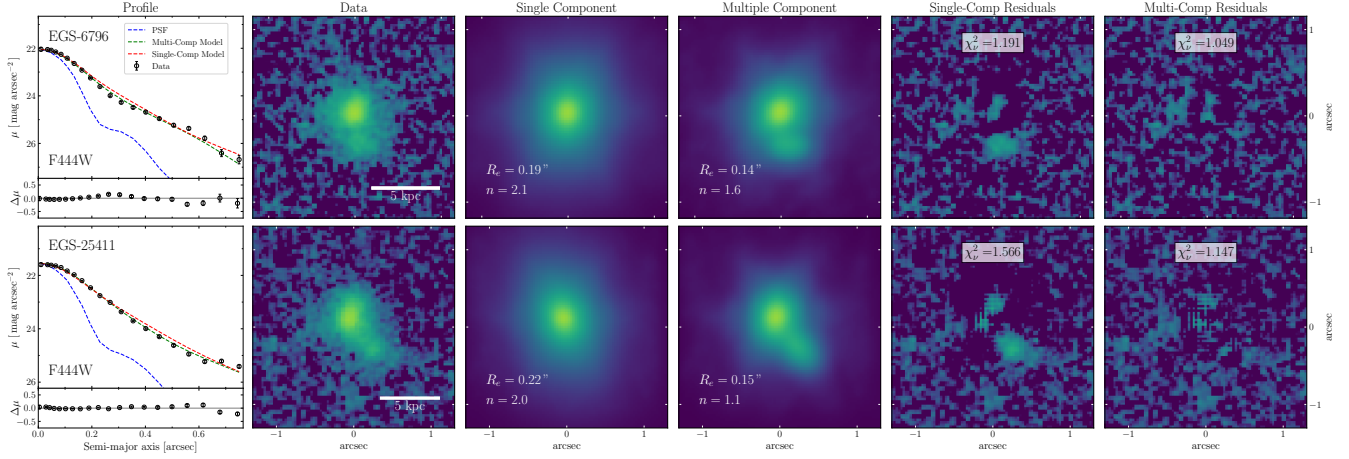


Figure 3. Treatment of blended sources, to avoid biased measurement of structural parameters caused by neighboring source contamination. In the 1D profile, the black points with error bars are measured by aperture photometry, the red dashed line shows the single-component model profile, green dashed line the multi-component model, which includes the target galaxy and the contaminating neighbor, and the blue dashed line represents the PSF, scaled to match the model profile. It is clear that the outer region of the target galaxy is heavily contaminated by the neighbor, and the additional component is necessary to measure the structural parameters of the target galaxy accurately. The images show, from left to right, the original image, the single-component model, the multi-component model, and the respective residuals for the two models.

to a bluer outskirts of the galaxy, which is quantified by $\mathcal{R} > 1$.

Additionally, we follow the definition in [Marian et al. \(2018\)](#), to define the color gradient ∇_{b-r} as:

$$\nabla_{b-r} = \frac{\Delta(\mu^b(R) - \mu^r(R))}{\Delta \log R}, \quad (4)$$

where the surface color profile $\mu^b(R) - \mu^r(R)$ is defined as the difference of surface brightness profile $\mu(R)$ between the blue band and the red band at radius R . The denominator $\Delta \log R$ is the difference of radius in the log scale. The formula shows the two-point slope of the color profile, which can be a good approximation of the color gradient between given radii R_1 and R_2 . By carefully examining the surface color profile of galaxies in our sample, we find that the choice of $R_1 = 0.1R_e$ and $R_2 = 1.2R_e$ can effectively capture the color gradients in the area with guaranteed signal-to-noise ratios.

In the following sections, we use structural parameters measured in F150W and F444W to quantify the radial variation of color. More specifically, we let the blue band be F150W and the red band be F444W in Equation 2, Equation 3, and Equation 4. The reason we use F444W in the reddest end is that we hope to extend the wavelength baseline as much as possible, to enhance the contrast fully. But in terms of the bluest end, for our redshift range, we usually see faint (due to severe dust attenuation) and clumpy (since the bluest end is usually dominated by star-forming clumps) structures in F115W. Considering our sources mostly have larger

than 5σ detection at HST/WFC3 F160W in [Stefanon et al. \(2017\)](#), the structure measurements in F150W are guaranteed. The measurements used for color gradient analysis can be found in Table A1.

To examine whether our quantification of the color gradient can describe the real observation well, we conduct a similar analysis based on our realistic mocks (as mentioned in Section 3.2), in pursuit of the limit of measuring the color gradient of the galaxies under observational constraints. We study our mock galaxies with different magnitudes and structural parameters especially the effective radius, by trying to reproduce the measurement \mathcal{R} , \mathcal{N} and $\nabla_{F150W-F444W}$ as an input-output experiment.

We mainly focus on galaxy sizes, namely to which extent we can precisely measure the multi-band morphologies for the smallest systems. Since our following analysis is based on resolved images across different bands, galaxies with small effective radii measured which are barely resolved ones should be excluded from the final sample. We divide galaxies into different size bins and consider their size variation (i.e., the input \mathcal{R}) across bands simultaneously. We present a detailed description of our mocks in Appendix B. The result shows that within the size of $0.04''$, the recovery of \mathcal{R} is biased. For the measurement of \mathcal{N} and ∇ , the size criteria are more stringent, where galaxies with $R_e < 0.06''$ can hardly be tolerated. The final size cut we choose is $R_e = 0.06''$, which is plausible as the PSF FWHM for NIRC2 images we use is between 0.06 to 0.16 arcsec ([Rigby et al.](#)

2023; Zhuang & Shen 2024). The size cut is applied for every band measurement to ensure that no bias is introduced: galaxies with positive color gradients may appear small in blue bands, and the same thing could happen for negative color gradients in red bands. As for magnitude cut, the trend that the measurement becomes more biased towards lower surface brightness and signal-to-noise ratio propels us to select galaxies that have a magnitude of at least 28 mag (< 28.0 mag). There are 120 galaxies beyond either size cut or magnitude cut. The following analysis uses all the galaxies with blendness flags 1 and 2 (as mentioned in Section 3.1), and within both size cut and magnitude cut, which correspond to 428 galaxies.

4.2. Rest-frame Color Inference

After selecting the sample of interest, we use **EaZY** to infer the rest-frame spectral energy distribution (SED), which is commonly used to derive rest-frame colors (e.g., Skelton et al. 2014; van der Wel et al. 2014b; Nedkova et al. 2024a). **EaZY** has been successful since its first release (Brammer et al. 2008), and has been widely used in various redshift ranges. The code gained its popularity not only for its accuracy but also for its simplicity of use, along with the flexibility in the choice of templates and implementation of physical priors. We use the Python version of **EaZY** (**eazy-py**³) in the following analysis.

Many works, including those of Wang et al. (2024) and Harvey et al. (2024), have agreed well that **tweak.fsps.QSF.12.v3** templates implemented with six new bluer templates described in Larson et al. (2023) can provide a more accurate estimation of photometric redshift at high redshift ($z \gtrsim 4$). Our setup of **eazy-py** is described as follows: First, we fix the redshift to the value in the CANDELS photometric redshift catalog. We add the new templates from Larson et al. (2023) to the default **tweak.fsps.QSF.12.v3** templates instructed by <https://ceers.github.io/LarsonSEDTemplates>. We combine our NIRCам measurement with existing photometry in the EGS field, ranging from optical (CFHT MegaCam) to mid-infrared (Spitzer). We apply an additional 10% relative error to our model flux to account for the systematic difference between our photometry and the method described in Stefanon et al. (2017). A Milky Way extinction of $E(B - V) = 0.006$ mag and $R_V = 3.1$ is adopted to correct for the foreground reddening.

eazy-py provides a basic estimate of rest-frame colors by interpolating (or extrapolating) the best-fit SEDs

for a given redshift to obtain the flux at filters such as rest-frame U , V , and J . We use these colors to further characterize our sample. The UVJ diagram (Williams et al. 2009) is a widely used tool to classify galaxies into different types based on their rest-frame colors. In Section 5.3, we show that our sample clustering on the lower left corner of the UVJ diagram, which indicates that our sample is mostly comprised of star-forming galaxies and they tend to be dustless.

5. RESULTS

5.1. Resolving Color Gradients

Galaxies exhibit negative color gradients if they have decreasing color profiles towards outer regions. Galaxies in our sample do show well-established negative color gradients, as **GalFitM** result shows either a positive slope of n or a negative slope of R_e with wavelength. In the left panel of Figure 4, we show a typical example of a galaxy with a negative color gradient, where the color profile gets bluer in the outskirts of the galaxy. For this galaxy, the blue band (F150W) refers to its rest-frame UV and the red band (F444W) refers to its rest-frame near-infrared. The galaxy has a larger R_e and smaller n in its rest-frame UV compared to rest-frame near-infrared, indicating a more extended star-forming counterpart which is bluer in color, and a compact region that is redder.

However, not all of the model predicts a monotonically decreasing color profile, as pointed out in Vulcani et al. (2014), the increasing n with a wavelength-independent R_e can also lead to an atypical scenario of negative color gradient: the galaxy is red in the center, blue in the middle, and red again in the outskirts. This is explained by the fact that the outer profile of the galaxy is usually hard to constrain, as the noise level increases with radius, which is confirmed by the stacked analysis. We define the edge of the galaxy as the radius where the Sérsic model profile has reached the background level, to serve as a reference for the region to define color gradient. We find that for most of the galaxies in our sample, the boundary is approximately 1.5-2.5 times R_e . So we choose to only consider the color gradient within $\sim R_e$, as defined in Section 4.1.

Galaxies exhibit positive color gradients if they have increasing color profiles towards outer regions. In our context, either a decreasing n or an increasing R_e with wavelength can lead to a positive color gradient. In the right panel of Figure 4, we display a typical example of a positive color gradient.

Since the science image is influenced by the PSF, which hinders the visualization of the color gradient, we apply PSF matching to the science image for bet-

³ <https://eazy-py.readthedocs.io/en/latest/>

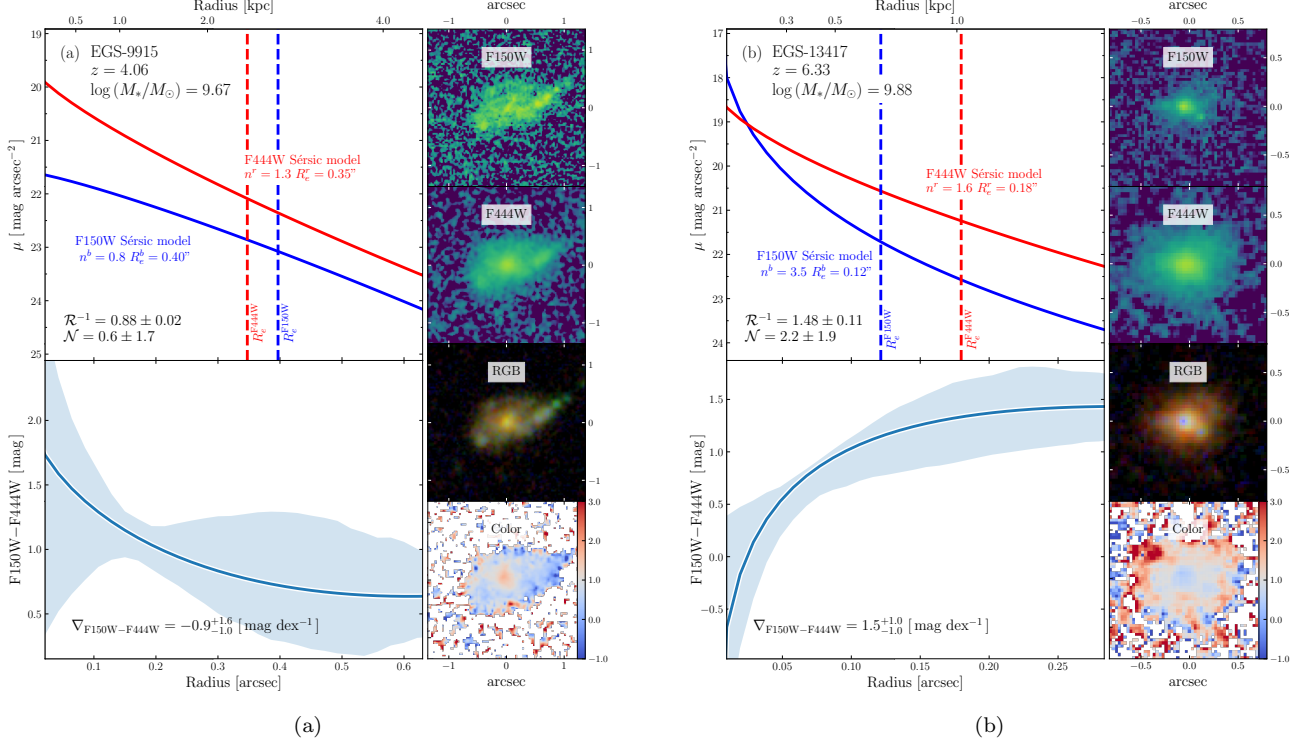


Figure 4. Example of a galaxy with (a) negative and (b) positive color gradient in our sample. In each panel, the left column shows the best-fit Sérsic model profile for the F150W and F444W bands (top) and the F150W–F444W color profile (bottom), where the blue shaded area shows the 16th and 84th percentile of the color profile derived by sampling the structural parameter according to its uncertainty. The right column of each panel shows the 2D visualizations of the color gradients: from top to bottom, the panels show the science images from F150W and F444W, the pseudo-color image (red = F444W, green = F277W, blue = F150W), and the PSF-matched F150W–F444W color image.

ter illustration. We assume a SplitCosineBellWindow kernel and use `create_matching_kernel` embedded in `photutils` to create a PSF matching kernel. The new kernel is then applied to the shorter wavelength band image to match the PSF of the longer wavelength. Finally, the color image is created by subtracting the PSF-matched images. The lower right panel in Figure 4 shows the PSF-matched color image of two galaxies, where the negative color gradient can be seen clearly. However, for the positive color gradient, the PSF-matched color image is less informative, as the more centrally concentrated light distribution in a shorter wavelength band can be smeared out by PSF more violently when compared to the extended morphology at the redder band. But even in this case, we can still discern the clear existence of the positive color gradient.

5.2. Dependency on Galaxy Properties

We then study the dependency of color gradients on galaxy properties, through our three proxies of color gradient: \mathcal{R} , \mathcal{N} and $\nabla_{F150W-F444W}$. $\nabla_{F150W-F444W}$ directly identify the color gradient. Though the first two measurements do not directly identify the color gradient,

they should provide basic implications while enjoying the privilege of being more robust and less sensitive to artificial effects introduced by the definition of color gradient. By combining the three proxies, we could study the color gradient and its dependency on galaxy properties comprehensively and robustly.

We show the dependency on galaxy sizes, stellar masses, and colors in Figure 5. In each subpanel, we calculate the running median to show the trend. Every bin includes at least 60 galaxies and the error bar indicates the scatter of the trend which is estimated from the standard deviation of the data points in each bin. In the first column, we use the effective radius measured at the rest-frame optical band as the galaxy size proxy. The rest-frame optical band refers to the band that has the closest effective wavelength to the rest-frame 5000 Å, which is summarized in Table A1.

We find a perceivable correlation between \mathcal{R}^{-1} and galaxy sizes, where galaxies with larger sizes in their rest-frame optical tend to exhibit a larger \mathcal{R} . This trend is robust when considering different size proxies (i.e., the effective radius measured in different bands, see discussion in Appendix C). The trend of \mathcal{R}^{-1} with stellar mass

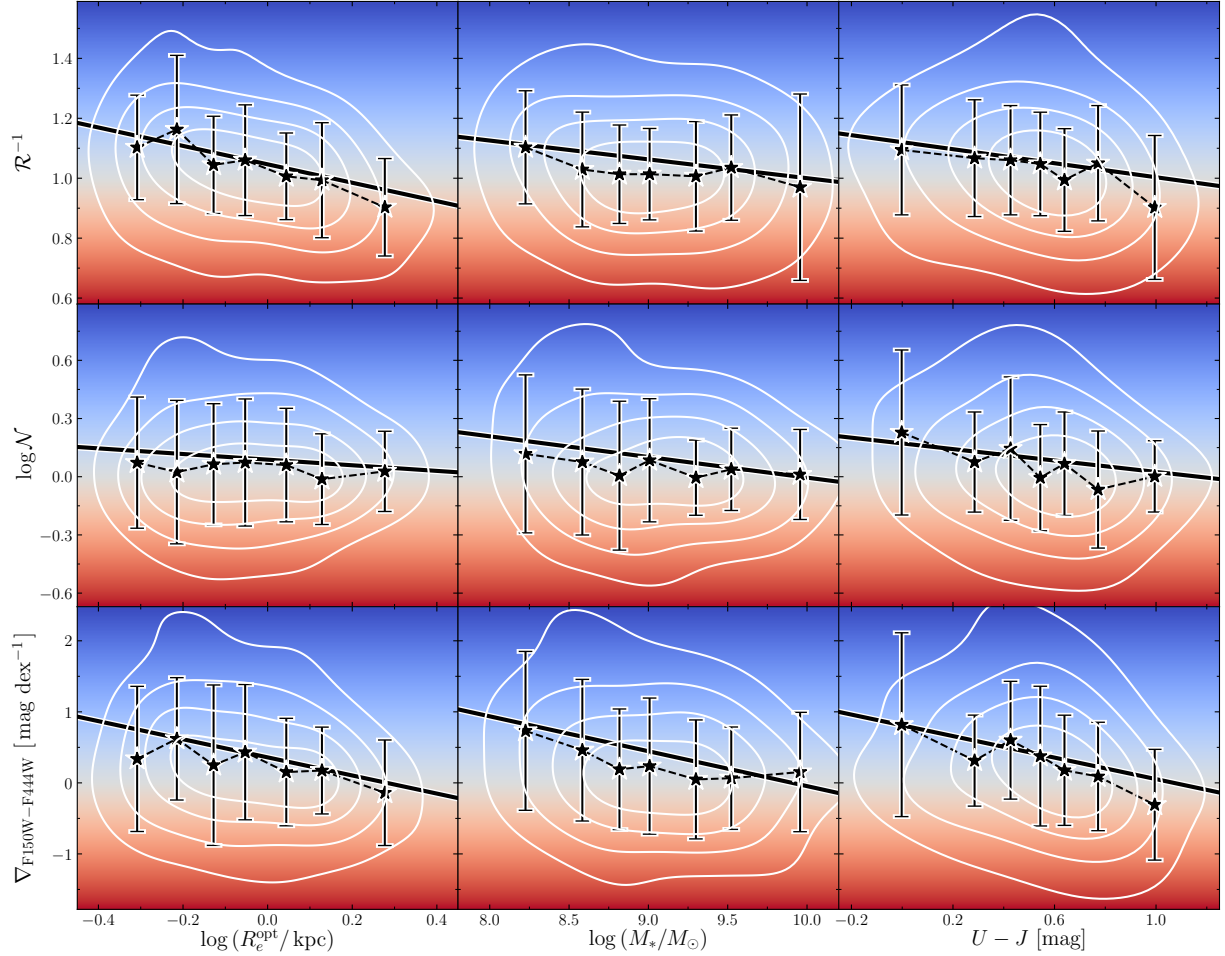


Figure 5. Dependence on galaxy properties of the color gradient, quantified using (top) the variation of the effective radius \mathcal{R} (Equation 3), (middle) variation of the Sérsic index \mathcal{N} (Equation 2), and (bottom) the color gradient $\nabla_{F150W-F444W}$ (Equation 4). From left to right, the columns show the dependence on galaxy optical effective radius (R_e^{opt}), stellar masses (M_*), and rest-frame $U - J$ color. The white contours denote the density distribution of the data points, the stars show the running median of the data binned so that each bin contains at least 60 galaxies, and the error bars indicate the standard deviation. The solid line gives the best-fit linear regression. The background gradient denotes the region where the color gradient is positive (blue) or negative (red).

is less steep. However, this flattened rising trend is robust in statistics with a p -value of 0.008 to accept the null hypothesis that there is no correlation, as illustrated in Table 1. The flattened slope can be explained by the relatively flat relation for SFGs in the mass-size plane (Ward et al. 2024), and also in the luminosity-size plane (Ono et al. 2024; Sun et al. 2024).

The variation of the Sérsic index with galaxy properties is hard to constrain, as measuring the Sérsic index is much more difficult than the effective radius, and the uncertainty is usually larger (Sun et al. 2024). We again conduct the same analysis as above, and since \mathcal{N} can span a larger range than \mathcal{R} (also see Vulcani et al. 2014), we opt to use the logarithm of \mathcal{N} to illustrate the trend better.

The middle part of Table 1 shows the best-fit result of linear regression for the dependency of $\log \mathcal{N}$ on galaxy properties. We found that \mathcal{N} is somewhat insensitive to galaxy sizes, as the slope is consistent with zero and the p -value is quite large. The dependency on stellar mass is robust, with a p -value smaller than 0.001, suggesting that for high-mass systems, the light profile is more likely to be flat in the bluer band, and steep in the redder one.

Interestingly, despite its insensitivity to galaxy sizes, the variation of n with galaxy color is somehow robust in statistics with a p -value of 0.001. As shown in the central subpanel in Figure 5, we found that \mathcal{N} is statistically sensitive to galaxy color: bluer galaxies tend to have larger n at bluer bands, whereas redder ones tend to exhibit early-type morphology at longer wavelengths.

By combining those fitting results, we can infer the dependency of color gradient on galaxy properties. We show that those large galaxies are exhibiting negative color gradients. The more galaxies have assembled, their sizes are more extended in bluer bands ($\mathcal{R} > 1$), while n shows no significant variation. On the other hand, when galaxies are smaller, their sizes are more compact at shorter wavelength ($\mathcal{R} < 1$), and with a subtle trend of \mathcal{N} , we can infer that those small galaxies are more likely to exhibit a positive color gradient. Similarly, we can conclude that for massive systems, negative color gradients are preferred, while for low-mass systems, positive color gradients are more likely to be seen. When considering the U-J color, we found that bluer galaxies tend to have larger \mathcal{N} ($\mathcal{N} > 1$) and smaller \mathcal{R} ($\mathcal{R} < 1$), which implies that they are more likely to be blue in the center and red in the outskirts. On the other hand, redder galaxies tend to have smaller \mathcal{N} ($\mathcal{N} < 1$) and larger \mathcal{R} ($\mathcal{R} > 1$), which indicates negative color gradients.

For the proxy $\nabla_{\text{F150W-F444W}}$, the result is consistent with what we have derived using \mathcal{R} and \mathcal{N} . As shown in the third row in Figure 5, positive color gradients tend to inhabit small-size, low-mass and blue systems, where galaxies with negative color gradients are generally larger, more massive and redder in color. Statistics in the lower part of Table 1 also shows significance for all three galaxy properties.

Furthermore, we visualize the dependencies on size-mass plane and color-mass plane in Figure 6. The trend is consistent considering different quantification of color gradient. Galaxies with negative color gradients tend to locate in the upper right corner of the panel, where the stellar mass and size (or $U - J$ color) is large. Galaxies with positive color gradients are more likely to be found in smaller and bluer systems with small stellar masses.

We try to examine if a certain type of color gradient inhabits galaxies with late-type or early-type morphology. However, no statistical evidence can be found from the regression of \mathcal{R}^{-1} on n^{opt} , which is the Sérsic index measured at the rest-frame optical band. The Sérsic index variation is also insensitive to n^{opt} according to regression (i) in Table 1, and the same conclusion is drawn for $\nabla_{\text{F150W-F444W}}$. Then, we explore the dependency of \mathcal{R}^{-1} , $\log \mathcal{N}$ and $\nabla_{\text{F150W-F444W}}$ on axis ratio. The correlation is not significant enough for \mathcal{R}^{-1} , as the slope is consistent with zero and the p -value is large. However, moderately robust evidence ($p = 0.035$) can be seen when considering the correlation of $\log \mathcal{N}$ on axis ratio, and $p = 0.046$ for the correlation of $\nabla_{\text{F150W-F444W}}$, as shown in Table 1. This leaves a hint that positive color gradients are more likely to be found for disk-like morphology or prolate systems (Tomassetti et al. 2016), as

Table 1. Best-fit Results of Linear Regression

Label	X	s	X_0	p -value
(1)	(2)	(3)	(4)	(5)
$\mathcal{R}^{-1} = s(X - X_0) + 1$				
(a)	$\log(R_e^{\text{opt}}/\text{kpc})$	-0.31 ± 0.07	0.15 ± 0.04	0.000*
(b)	$\log(M_*/M_\odot)$	-0.06 ± 0.02	10.00 ± 3.98	0.008*
(c)	$U - J$ (mag)	-0.12 ± 0.03	1.03 ± 0.30	0.001*
(d)	Axis ratio	-0.07 ± 0.08	1.36 ± 1.69	0.420
(e)	$\log n^{\text{opt}}$	0.08 ± 0.06	-0.65 ± -0.47	0.163
$\log \mathcal{N} = s(X - X_0)$				
(f)	$\log(R_e^{\text{opt}}/\text{kpc})$	-0.15 ± 0.09	0.61 ± 0.42	0.126
(g)	$\log(M_*/M_\odot)$	-0.11 ± 0.03	9.96 ± 3.84	0.000*
(h)	$U - J$ (mag)	-0.15 ± 0.04	1.17 ± 0.40	0.001*
(i)	Axis ratio	-0.23 ± 0.11	0.91 ± 0.50	0.035*
(j)	$\log n^{\text{opt}}$	0.13 ± 0.07	-0.62 ± -0.37	0.069
$\nabla_{\text{F150W-F444W}} = s(X - X_0)$				
(k)	$\log(R_e^{\text{opt}}/\text{kpc})$	-1.27 ± 0.29	0.28 ± 0.08	0.000*
(l)	$\log(M_*/M_\odot)$	-0.49 ± 0.09	9.91 ± 2.51	0.000*
(m)	$U - J$ (mag)	-0.76 ± 0.13	1.07 ± 0.22	0.000*
(n)	Axis ratio	-0.67 ± 0.33	1.12 ± 0.62	0.046*
(o)	$\log n^{\text{opt}}$	0.11 ± 0.22	-3.71 ± -7.74	0.632

NOTE— Col. (1): The label of the linear regression. Col. (2): The galaxy property that serves as the independent variable X in the regression. Col. (3): The best-fit slope of the linear regression. Col. (4): The typical value X_0 of the independent variable X that makes the estimated variation (i.e., the estimated value of \mathcal{R} or \mathcal{N} at X_0) equals 1. For $\nabla_{\text{F150W-F444W}}$, X_0 refers to the typical value that makes $\nabla_{\text{F150W-F444W}} = 0$. Col. (5): The probability of accepting the null hypothesis that the slope is zero (i.e., no statistical correlation). *We take p -value < 0.05 as the probability of rejecting the null hypothesis of no correlation.

these two scenarios usually correspond to smaller values of axis ratio. We will discuss its physical implications further in Section 6.1.

5.3. The Rest-frame SEDs of Negative and Positive Color Gradients

We show the distribution of our sample in the UVJ diagram in Figure 7. U , V , J colors are inferred from EAzy template fitting as mentioned in Section 4.2. The UVJ diagram could be a good indicator of the origin of the color gradients (Wang et al. 2017; Miller et al. 2022, 2023) since it basically characterizes the shape of SED, which is closely related to the star-forming activity and dust attenuation. The lower left corner of the UVJ diagram is usually occupied by star-forming galaxies with little dust attenuation, because of the blue stellar population and the steep UV slope.

To investigate whether the observed radial color variation is originated from the spatial distribution of dust, we conduct a simple analysis by quantitatively separating galaxies into three categories of color gradients based

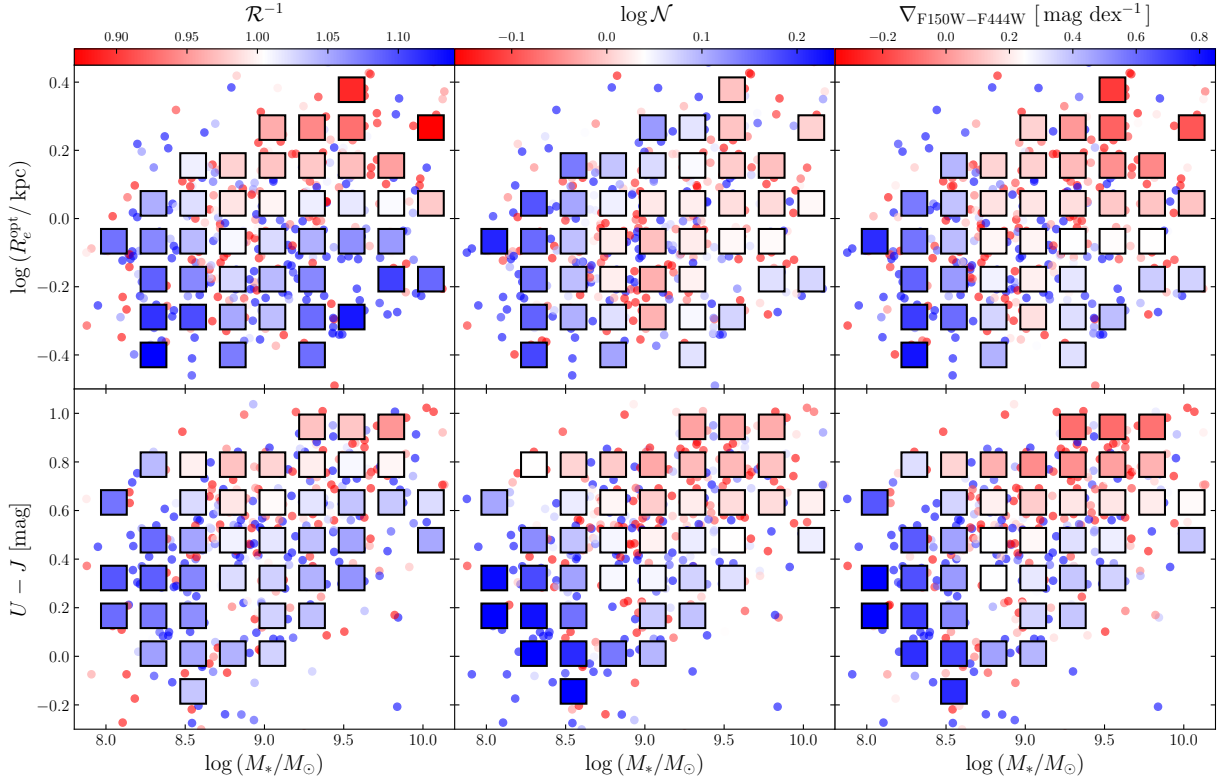


Figure 6. The stellar mass-size and stellar mass-color plane of our sample. From left to right, the columns quantify the color gradient using \mathcal{R}^{-1} , $\log \mathcal{N}$, and $\nabla_{\text{F150W-F444W}}$, whose strength is indicated by the color bar on the top. The squares denote median values of at least five objects within a box of size 0.25 dex in $\log M_*$ and 0.11 dex in $\log R_e^{\text{opt}}$ or 0.15 mag in $U - J$, after performing a locally weighted regression smoothing using the Python package LOESS (Cappellari et al. 2013).

on $\nabla_{\text{F150W-F444W}}$. We introduce a fiducial threshold of $|\nabla_{\text{F150W-F444W}}| = 0.5$ [mag/dex], where the sample with $\nabla_{\text{F150W-F444W}} < -0.5$ [mag/dex] is robustly considered as a galaxy with negative color gradient (∇ -NCG). The sample with $\nabla_{\text{F150W-F444W}} > 0.5$ is therefore robustly considered as a galaxy with a positive color gradient (∇ -PCG). For galaxies that have $-0.5 \leq \nabla_{\text{F150W-F444W}} \leq 0.5$, we conservatively define them as galaxies with little evidence of color gradients or flat color gradients.

The overall distribution of our sample in the UVJ diagram mostly corresponds to the dustless star-forming galaxy. ∇ -NCGs are located slightly on the upper right side of ∇ -PCGs. This is consistent with our previous result (Section 5.2) that positive color gradients are more common in galaxies with bluer color. As for ∇ -NCGs, they are inclined to be more dust attenuated, as the color is redder, which leaves a hint that the negative color gradient can also be associated with dust at $z > 4$.

However, since the rest-frame J band cannot be covered by the longest wavelength band (F444W) of JWST NIRCcam for galaxies in our sample at $z > 4$, the only constraint on the rest-frame J magnitude comes from Spitzer photometry, which suffers from lower resolu-

tion as well as lower sensitivity than JWST. Therefore, the rest-frame J magnitude has a larger uncertainty (a larger median errorbar in rest-frame $V - J$ color in Figure 7). To mitigate this issue, MIRI photometry could be used in further analysis to constrain the rest-frame near-infrared SEDs at $z > 4$.

To further emphasize the color difference between our sample of NCGs and PCGs, we reveal the SED shapes of the two populations with `eazy-py` in their rest-frame UV-to-NIR, as this wavelength range has been well captured by the broadband photometry from JWST/NIRCcam with guaranteed constraining power. The rest-frame spectrum for either PCGs or NCGs is calculated using the best-fit templates for each galaxy at the given redshift. At every rest-frame wavelength grid, we take the median value of the galaxies' best-fit template distribution as the SED (solid lines), and estimate the scatter of each distribution using the 16th and 84th percentile of the flux density. As illustrated in the top panel of Figure 8, PCGs are more luminous in their rest-frame UV, and a redder SED shape can be discerned for NCGs.

To ensure that the mean observed SED shapes are not biased due to the wide range of stellar mass, we show

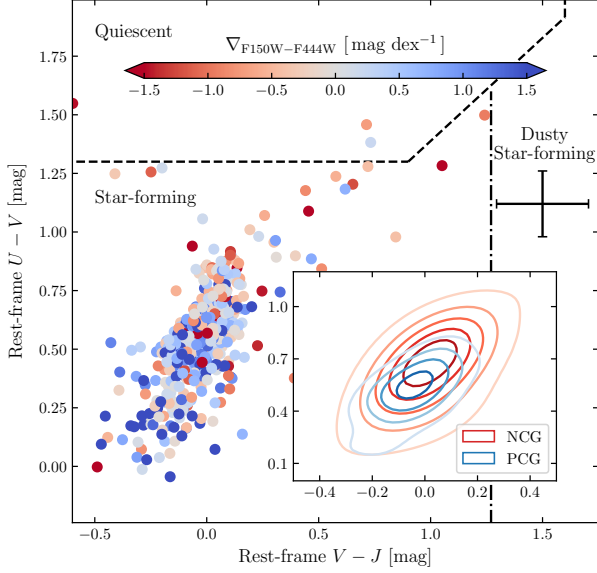


Figure 7. UVJ diagram for the galaxies in our sample, color-coded by $\nabla_{F150W-F444W}$ (Equation 4), whose strength is indicated by the color bar. The dashed lines are the criteria for separating star-forming and quiescent galaxies (Williams et al. 2009), while the dot-dashed line defines the dusty star-forming galaxies (Miller et al. 2023). The inset subpanel shows the kernel density estimation of the population with negative color gradient (NCG; red contours) and positive color gradient (PCG; blue contours). The error bars indicate the median value of uncertainties of the rest-frame colors, as inferred using *eazy-py* (Section 4.2).

the rest-frame SED shapes of the two populations in different stellar mass bins on the lower panels of Figure 8. There is evidence that at the high stellar mass bin ($M_* \geq 10^9 M_\odot$), NCGs feature more prominent Balmer breaks compared to those positive color gradients, indicating an older stellar population. For massive systems, the median SED of PCGs shows much stronger UV emission, which may imply a recent intense star formation. We are cautious that the statistical significance is weak when considering low stellar mass samples, as the sample size is quite limited (only 31 NCGs with $M_* < 10^9 M_\odot$) and the measurement error is large. However, the trend is still perceivable, and statistically significant in massive galaxy bins.

To further emphasize the color difference between our sample of ∇ -NCGs and ∇ -PCGs, we reveal the SED shapes of the two populations with JWST NIRCcam data points. We opt not to include other photometry, as NIRCcam photometry has the best data quality and the wavelength coverage is already sufficient to illustrate the trend.

We show the mean SED shapes of the two populations in Figure 9, where ∇ -PCGs are more luminous in

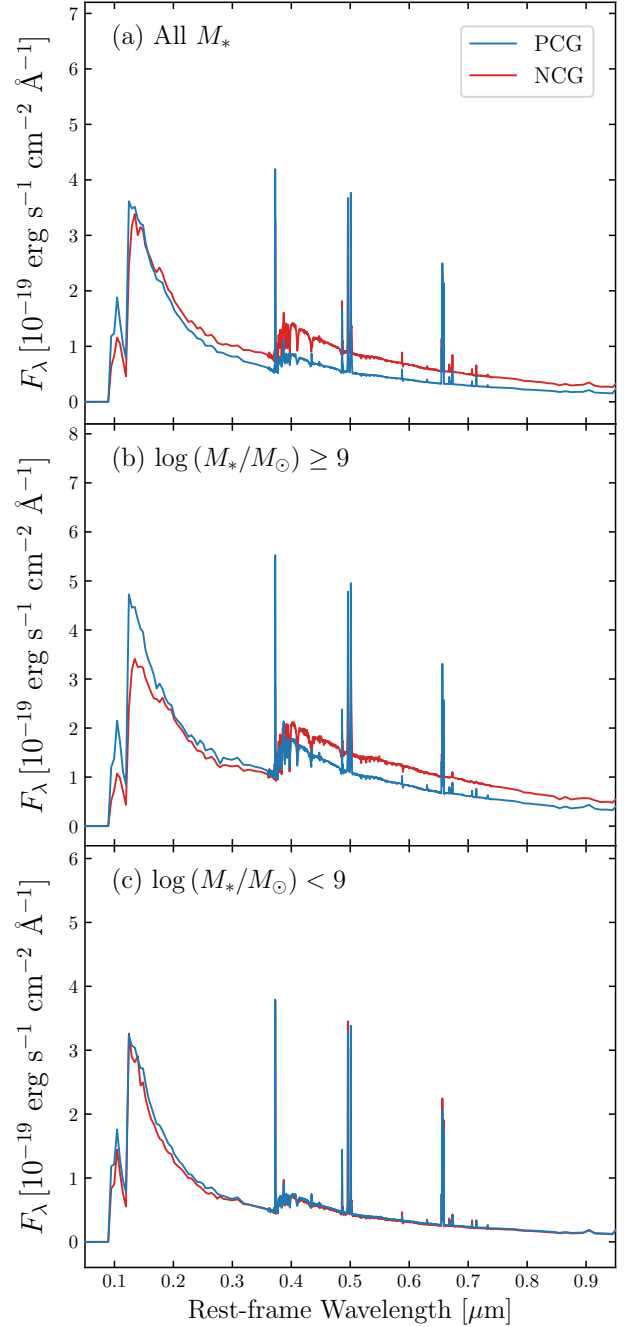


Figure 8. The rest-frame SEDs of galaxies with negative color gradient (NCG; red) and positive color gradient (PCG; blue). The top panels show the entire sample, and the lower panels are divided by the stellar mass threshold of $\log(M_*/M_\odot) = 9.0$. The solid lines are the median value of the best-fit template spectra for each group of galaxies and the shaded area shows its 16th and 84th percentile of the galaxy distribution.

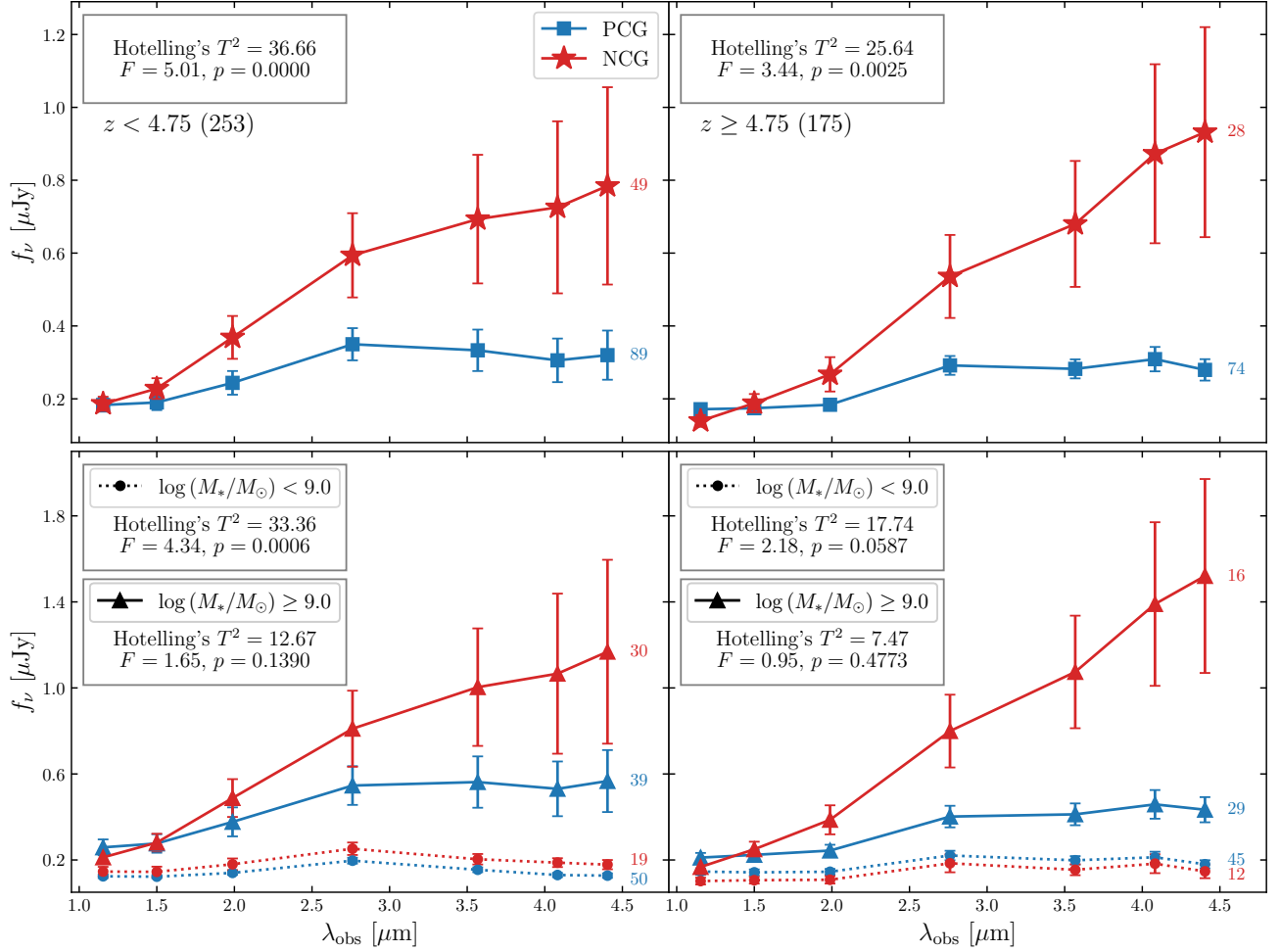


Figure 9. The mean observed SEDs of galaxies with negative color gradient (NCG; red) and positive color gradient (PCG; blue), divided into redshift bins $z < 4.75$ (left) and $z \geq 4.75$ (right). The top panels show the entire sample, and the lower panels are divided by the stellar mass threshold of $\log M_* = 9.0$. The number on the right of each SED indicates the galaxy number in each bin. Assuming that the measured flux is sampled randomly from a Gaussian distribution $N(f_{\nu_i}, \sigma_i)$, we derive the error bar as the standard error of the estimated mean flux $SE(f_{\nu_i}) = \sigma_i/\sqrt{N}$, where σ_i is the standard deviation of the i -th band flux and N is the number of galaxies in each bin. The text box in each panel gives the basic statistics used to infer the significance of the difference between the two SEDs.

their rest-frame UV, and a redder SED shape can be discerned for ∇ -NCGs. This is consistent with our expectation that the positive color gradient is more likely to be associated with intense central star formation thus luminous rest-frame UV color, and the negative color gradient can be related to more dust attenuation and older main stellar population.

We have also checked the statistical significance of their SEDs by conducting a Hotelling's T^2 test, which is a multivariate generalization of the t test. Hotelling's T^2 test is commonly used to compare the means of multivariate populations in two-sample statistics. It allows us to test the difference in the SED shapes of the two populations even if the difference of each single band flux is not statistically significant. The null hypothesis

is that for every band, observed flux densities f_{ν} of the two populations are drawn from the distribution with the same mean:

$$f_{\nu_i}^{\nabla\text{-PCG}} = f_{\nu_i}^{\nabla\text{-NCG}}, \quad i = 1, 2, \dots, N, \quad (5)$$

where $f_{\nu_i}^{\nabla\text{-PCG}}$ and $f_{\nu_i}^{\nabla\text{-NCG}}$ are the mean observed flux densities of the two population distributions in the i -th band, and N is the number of bands, which is 7 in our case.

We calculate Hotelling's T^2 statistic, which is tightly related to the F -statistic if assuming the sample is drawn from a Gaussian distribution, and the p -value is calculated based on the F -distribution. Since our sample spans a wide range of redshift, the redshifted SED that we observed is quite distinct (e.g., the band flux ob-

Table 2. Redshift Evolution of Color Gradient

Redshift	Number	\mathcal{R}^{-1}	$\log \mathcal{N}$	$\nabla_{\text{F150W-F444W}}$
(1)	(2)	(3)	(4)	(5)
$4 \leq z < 4.35$	130 (4.18)	$0.96^{+0.19}_{-0.12}$	$0.07^{+0.31}_{-0.20}$	$0.15^{+0.92}_{-0.74}$
$4.35 \leq z < 4.85$	148 (4.59)	$1.05^{+0.26}_{-0.20}$	$0.07^{+0.45}_{-0.3}$	$0.26^{+1.73}_{-0.78}$
$4.85 \leq z < 8.0$	150 (5.34)	$1.06^{+0.16}_{-0.25}$	$0.01^{+0.35}_{-0.25}$	$0.22^{+0.94}_{-0.74}$

NOTE— Col. (1): Redshift Range. Col. (2): Number of galaxies in each redshift bin (with the median redshift value in the parenthesis). Col. (3): The median value of the color gradient proxy \mathcal{R}^{-1} , and the 16-th and 86-th percent of the distribution. Col. (4): The median value of the color gradient proxy $\log \mathcal{N}$, and the 16-th and 86-th percent of the distribution. Col. (5): The median value of the color gradient proxy $\nabla_{\text{F150W-F444W}}$, and the 16-th and 86-th percent of the distribution.

served in F200W will belong to rest-frame optical and rest-frame UV for galaxies at redshift $z < 4.75$ and $z > 4.75$ respectively). We separate our sample into 2 redshift bins by $z = 4.75$ for the statistic tests. We end up with p -value of 6.4×10^{-5} and 0.0025 for $z < 4.75$ and $z \geq 4.75$ respectively, which is statistically robust to reject the null hypothesis, indicating that the SED shapes of the two populations are significantly different. We have also checked the robustness of the result by altering the threshold of the definition of ∇ -PCG and ∇ -NCG, and the result is still consistent.

To ensure that the mean observed SED shapes are not biased due to the wide range of stellar mass, we show the SED shapes of the two populations in different redshift and stellar mass bins on the lower panel of Figure 9. We are cautious that the statistical significance is weak when considering low stellar mass samples, as the sample size is quite limited (12-50 galaxies in each bin) and the measurement error is large. On the other hand, the trend is still perceivable, and statistically significant in massive galaxy bins.

5.4. Redshift Evolution of Color Gradient

In Figure 10, we show the redshift evolution of color gradient for our sample at $4 < z < 8$, with each row indicating a different proxy. As the measurement error increases towards high redshift, we opt to bin galaxies based on the median error of the measurement. We finally choose to divide galaxies into 3 redshift bins: (1) $4 \leq z < 4.35$; (2) $4.35 \leq z < 4.85$; (3) $4.85 \leq z < 8$, where the median error of each bin is 2-3 times smaller than the scatter, and the sample number is almost equally divided (Table 2). The values shown in Figure 10 are summarized in Table 2.

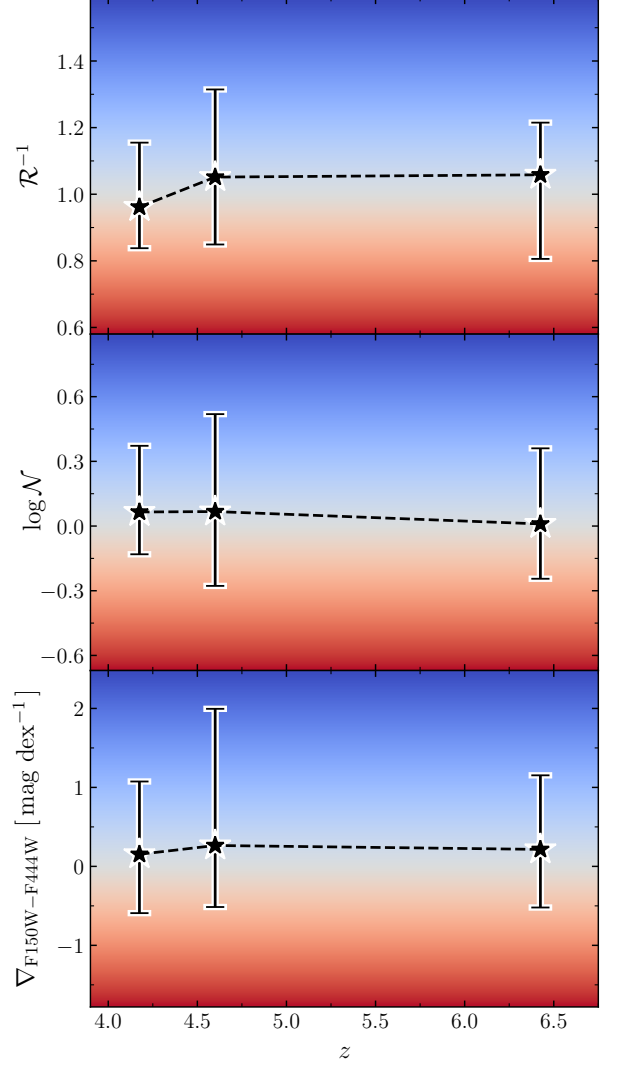


Figure 10. The redshift evolution of the color gradient, quantified using (top) the variation of the effective radius \mathcal{R} (Equation 3), (middle) variation of the Sérsic index \mathcal{N} (Equation 2), and (bottom) the color gradient $\nabla_{\text{F150W-F444W}}$ (Equation 4). The black stars indicate the median value for each redshift bin, with the error bar giving the 16-th and 84-th percentile of the distribution. The background gradient describes the region where the color gradient is positive (blue) or negative (red).

The result suggests both galaxies with negative color gradients and positive gradients are common at high redshift ($z > 4$). We also perceive a mild increase in the median value of our color gradient proxy \mathcal{R}^{-1} , and an even milder decrease of $\log \mathcal{N}$, while the evidence for the redshift evolution of $\nabla_{\text{F150W-F444W}}$ can be hardly discerned. This is reasonable because the time span between $4 < z < 8$ is relatively short (the corresponding age of the Universe is 0.646-1.558 Gyr). Since our current sample is deficit at the high redshift end, we cannot

draw a very safe conclusion as to whether or not the positive color gradient is becoming more dominant towards high redshift at the current stage.

6. DISCUSSION

6.1. Implication for Central Star Formation

While confirming the common existence of positive color gradients at $z \gtrsim 4$, in Section 5.2, we also find evidence for an excess of positive color gradients towards smaller galaxy sizes, low stellar masses, and bluer colors. These results raise an intriguing question: what is the physical nature of these positive color gradients?

Similar phenomena about the incidence of positive color gradients have been discovered at $z \approx 2$ in massive systems ($M_* \approx 10^9 - 10^{10} M_\odot$), where the central star formation is enhanced through “compaction” (Zolotov et al. 2015). Violent disk instability, minor mergers, and counter-rotating streams are proposed to be the triggers of the central starburst. At $z \lesssim 2.5$, MIRI observation has shown its superiority in tracing dust-obscured star formation, and decisive clues for massive galaxies experiencing the “compaction” phase were found (Magnelli et al. 2023; Lyu et al. 2024). Even at the local Universe, Tuttle & Tonnesen (2020) identified 118 “BreakBRDs” (break bulges in red disks) in face-on galaxies ($z < 0.05$) from the Sloan Digital Sky Survey (York et al. 2000), featuring truncated disk star formation and blue star-forming core. The misalignment and lack of angular momentum are found to be contributing to the central concentration of the dense, star-forming gas (Tonnesen et al. 2023; Stark et al. 2024). Cheng et al. (2020) selected low-mass ($\lesssim 10^{10} M_\odot$) systems at $0.05 < z < 0.3$ from the GOODS-North field, and discovered signs of “outside-in” growth pattern using UV-NIR size comparison, which leaves a hint that their high- z progenitors may be going through a similar process (Overzier et al. 2010).

Though the spatial distribution of young massive stars and redder populations are not well distinguished at $z > 4$ yet, the stochastic star formation history of high-redshift galaxies (Tacchella et al. 2020; Sun et al. 2023; Looser et al. 2024) may contribute to the origin of the positive color gradient. Many recent works have declared a prevalence of compact UV morphology in high-redshift galaxies (e.g., Harikane et al. 2024). Similar to lower redshift ($z \approx 2$), the bright UV luminosity nature of those compact systems can reveal the presence of a violent central star formation (central starburst) possibly being triggered by angular momentum dissipation originated by merger events or in-situ instabilities (Dekel et al. 2020). It’s worth noticing that in our sample, we perceive more positive color gradients at stellar

mass $M_* \lesssim 10^9 M_\odot$, which refers to the phase where there are more disruptive behaviors happening on the gas-rich disk (Tacchella et al. 2016; Dekel et al. 2020), and result in the violent central star formation. Observational evidence also includes Tripodi et al. (2024): at $4 \leq z \leq 10$, the central star formation is more intense in low-mass galaxies from JADES. The equivalent width of line emission peaks at the center and a tentatively inverse gas-phase metallicity gradient is discerned.

We also discover more positive color gradients for galaxies with lower stellar masses and smaller axis ratios. This is predicted by cosmological simulations, as the lower-mass objects that form stars in the center tend to be prolate systems (Lapiner et al. 2023). In the prolate system, the torque exerted by the triaxial geometry of the gravitational well can explain the efficient dissipation of angular momentum. This results in concentrated star formation and positive color gradients. Since there will be no direct clues to individually identify those galaxies with small axis ratios to be 3D prolates without dynamical information, even though many works have claimed the potential existence and prevalence of prolates at high- z (van der Wel et al. 2014a; Zhang et al. 2019; Pandya et al. 2024), we are cautious that we cannot draw solid conclusions here.

However, for small systems, it is often hard to constrain their structural parameters (especially n) for the following reasons: 1) the PSF effect is more severe for smaller galaxies, and the pixels available for the fitting are limited. 2) smaller galaxies tend to be fainter, which can be more affected by the noise. 3) if the faint stellar component behind the clumpy UV structure is underexposed, thus below the noise level, our measurement in the rest-frame UV band will be biased towards the smaller and more concentrated side. Also, the sample size is limited so far. Therefore, our conclusion about color gradients and their dependencies on galaxy properties is tentative at the current stage.

6.2. The Role of Active Galactic Nuclei

Apart from the role of the stellar population, whether or not the galaxy hosts active galactic nuclei (AGN) can affect our measurement if the central point-like source cannot be well modeled by the single Sérsic fit. The compact UV emission characteristic can be a sign of unobscured AGN, which can also provide a plausible explanation: A blue AGN can be prominent in blue bands compared to its host galaxy and combined with the point-like nature, the light profile of blue band image should be more concentrated in the center, thus leading to a positive color gradient. On the other hand, if the

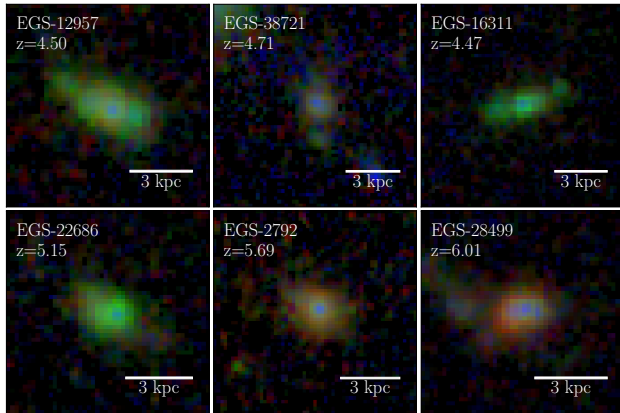


Figure 11. Pseudo-color images of galaxies with positive color gradients that show evidence of hosting a central point-like source. where red = F444W, green = F277W, and blue = F150W).

AGN is reddened by dust, the light profile should be more concentrated at a longer wavelength.

Mannerling et al. (2011) compared radio-loud AGNs with a control sample of radio-quiet galaxies in SDSS and discovered a central blue excess for AGN-host galaxies. The presence of radio-loud AGN is believed to enhance star formation within the central few kpcs. Though they ruled out the possibility that the AGN light can contribute to the central blue excess, the scenario should be reassessed for our sample at high redshift, where galaxies are smaller.

The recent JWST observations reveal an abundant number of high- z AGNs that can be bright in their rest-frame UV, along with their canonical optical continuum (e.g. Kokorev et al. 2024; ?). These broad-line AGNs (BLAGNs) featuring the V-shape SED in their rest-frame UV-to-optical, are referred to as little red dots (LRDs; Matthee et al. 2024). However, the origin of their bright UV continuum is still under debate. Previous studies argued that combining a reddened AGN with the scattered light of the accretion disc can provide a possible explanation for their intriguing V-shape SED (?), while Li et al. (2024) explained it with the flat UV extinction curve due to the absence of small-size dust grains. Apart from the AGN-only speculations, the simultaneous buildup of compact stellar populations can also contribute to the blue UV characteristics (Akins et al. 2024), and may even explain the detected broad lines without an AGN for LRDs with Balmer breaks (Baggen et al. 2024).

By carefully inspecting every single *GalfitM* fit result and color profile of our sample, we find 27 galaxies (6.3% of 428 galaxies) featuring central point-like emission, which are labeled with the potential AGN-host galaxy

flag shown in Table A1. We find 78% (21/27) of them exhibit positive color gradients, and 22% (6/27) exhibit negative color gradients. Figure 11 shows 6 examples of positive color gradients in RGB images. Notice that the last source EGS-28499 refers to CEERS.00397 in Harikane et al. (2023), which is identified to host a broad-line AGN by JWST/NIRSpec, but not categorized as a little red dot according to Taylor et al. (2024). Though the PSF FWHM is smaller at the bluer band, we confirm their point-like nature by implementing a PSF component in the *GalfitM* setup. In Figure 12, we show an example that our measurement of the color gradient is affected by the central point-like source: the color gradient proxy \mathcal{N} in this case flip inverse, turning the host galaxy into a negative color gradient. By including a PSF component in the model, the residual becomes cleaner, and the Sérsic index variation is not as drastic as before.

In terms of science, we opt not to exclude the 27 sources from the integrated analysis above, since the color gradient itself can originate from several physical reasons including the AGN. However, as the number of central point-like sources discerned for our sample is quite small, we confirm that the results are still robust after excluding every potential AGN identification, which indicates that the stellar population is still the major explanation of the observed color gradient characteristics.

However, the main shortcut is that it is challenging to distinguish AGN from young nuclear star clusters or even tiny young bulges without necessary spectroscopic information: the star-forming clumps can masquerade as AGN if their physical scale is small. Even if we can discern whether or not these objects are BLAGNs, we are still uncertain about the nature of their compact UV emission. As discussed above, it could either originate from the disc of an unobscured AGN (or the scattered light of the accretion disc), or the compact stellar emission alongside the SMBH. Under the circumstances, we expect to examine the scenario exhaustively with more spectral information in the future.

6.3. Comparison with Previous Studies

Our main results are basically consistent with previous studies, where the discrepancy between the rest-frame optical and UV sizes is less pronounced at $z > 4$ compared to lower redshift. The neutral distribution of the color gradient seems to contradict the larger UV sizes at $z \lesssim 3$ reported in many previous works (e.g., van der Wel et al. 2014b; Shibuya et al. 2015). This is not surprising though, as our findings can be compatible with the trend revealed by Suess et al. (2019), where the half-mass ra-

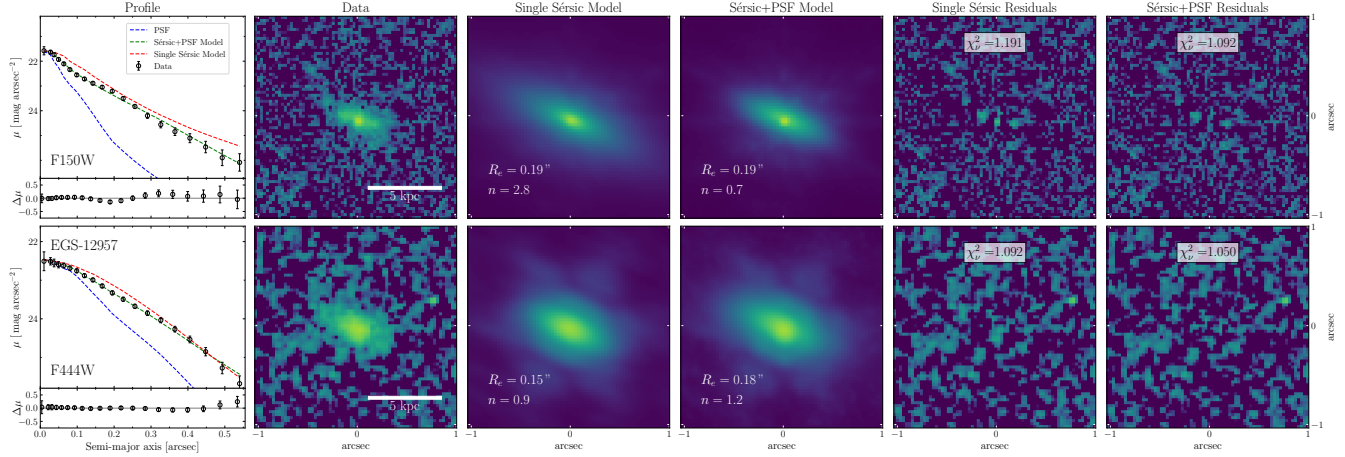


Figure 12. Influence of a “blue nucleus” on the measurements, for F150W (top) and F444W (bottom). In the 1D profile, the black points with error bars are measured by aperture photometry, the red dashed line shows the single-Sérsic model profile, the green dashed line the Sérsic plus point source model, and the blue dashed line represents the PSF, scaled to match the model profile. The lower panel of the left column shows the residuals between the Sérsic+PSF model and the data. The images show, from left to right, the original image, the single-Sérsic model, the Sérsic+PSF model, and the respective residuals for the two models. It is clear that including the PSF component improves the quality of the fit, and that the additional component is necessary to measure accurately the structural parameters of the host galaxy.

dius of galaxies is increasing to emulate half-light radius starting from $z = 1$ to $z = 3$, leaving little room for negative color gradients to be well established at $z \gtrsim 4$.

From the analysis in Section 5.2, galaxies with large sizes and stellar masses tend to exhibit negative color gradients, which follow the inside-out growth. Massive systems tend to exhibit steeper negative color gradients than low-mass systems, possibly because they have an older main stellar population, more metal enrichment, and more dust attenuation on average. The generally enhanced negative color gradient towards larger size and stellar mass has also been discovered at lower redshift with larger sample sizes. Nelson et al. (2016) found an increasing size discrepancy between the $H\alpha$ and stellar continuum morphology from 10^9 to $10^{11} M_\odot$. Suess et al. (2019) found that the strength of negative color gradient is stronger for the galaxy with larger size, larger stellar mass, and redder color. Despite the declaration that the trend is diminishing towards $z = 2.5$, it is still discernible in our analysis at $z > 4$. They also found no strong dependency of color gradient on the Sérsic index, especially in high- z bins, which is consistent with our result at $z > 4$. Apart from the inside-out growth for massive systems, the relatively flat color profile perceived for galaxies at intermediate stellar mass ($M_\star \approx 10^9 M_\odot$) can also be related to the “self-similar” assembly pattern, where star formation activities happen simultaneously across all radii for the certain stellar mass range (van Dokkum et al. 2013; Tacchella et al. 2018; Nelson et al. 2021; Hasheminia et al. 2024).

Our measurement can be compatible with the studies that focused on the Sérsic index variation as well. Martorano et al. (2023) reported that at lower redshift, star-forming galaxies have a mildly larger Sérsic index measured in $1.1\mu\text{m}$ than in $0.5\mu\text{m}$, but the trend disappears at $1.5 < z < 3$. However, they found no significant correlation between the Sérsic index variation and stellar mass, while in our sample the dependency is statistically robust. We speculate that it is because of the different range of stellar mass, whereas in our sample we include more low-mass systems that are more likely to possess positive color gradients, as pointed out in Section 5.2.

Moving towards higher redshift ($z \gtrsim 4$), our result is also suggestive of the independence of structural parameters on wavelength reported by Treu et al. (2023). The distribution is also consistent with Morishita et al. (2024): an overall neutral distribution with a slight tilt towards compact UV morphology can be seen. Additionally, when dividing into different redshift bins, we find that the distribution of \mathcal{R}^{-1} is exceeding unity mildly, with larger scatters at higher redshift, which may imply more abundant populations of positive color gradients and more diverse patterns of galaxy assembly at $z \gtrsim 5$. This is again consistent with the trend reported in Ono et al. (2024), where their sample of 149 galaxies is selected by the photometric redshift and drop-out technique.

7. SUMMARY

In this work, we present a comprehensive study of color gradients in high-redshift galaxies using the NIR-

Cam imaging data from the JWST CEERS survey. We obtain structural parameters of 669 galaxies at $4 < z < 8$ with **GalfitM**, which provides physically intuitive measurement by simultaneously fitting the multi-wavelength images. We have carefully examined the dependency of n and R_e on wavelength, in pursuit of characterizing the color gradient since the epoch of reionization. Our main results are summarized as follows:

1. We apply the parametric methodology of measuring galaxy color gradients out to $z > 4$, and consolidate the measurement through realistic mocks. We confirm that both positive and negative color gradients are common at $z > 4$, and provide a preliminary attempt to characterize and visualize those color gradients.
2. We find a distinguished correlation between the 3 color gradient proxies ($\mathcal{R}, \mathcal{N}, \nabla_{F150W-F444W}$) and galaxy sizes, and a milder correlation with stellar mass: galaxies with larger size and stellar mass tend to be actively forming stars on the outskirts. These galaxies also show distinct SED shapes compared to positive color gradients.
3. We discover an excess of galaxies with positive color gradients, especially for the smallest and bluest systems. This can be explained by episodic central burst and strong emission features triggered by prevalent angular momentum dissipation perceived at high redshift.
4. We only identify a relatively small number of galaxies (6.3%) with negative/positive color gradients that feature central point-like emission. By excluding every potential AGN identification, the main results remain the same. The stellar emission is the major driver of the excess of the positive color gradient, corresponding to a high incidence of central star formation.
5. Within the limitations of the current sample size, we claim no redshift evolution of color gradient at $4 < z < 8$, as the redshift trend inferred from the 3

proxies of color gradient is not significant enough to be discerned.

Future work can be improved in several directions. First, the sample size can be enlarged by including more galaxies from other JWST deep surveys available, such as JADES (Eisenstein et al. 2024), NGDEEP (Bagley et al. 2024), COSMOS-Web (Casey et al. 2023). Since our sample is mostly comprised of galaxies with bright H band magnitude, it can be biased towards the more dustless side, and the inclusion of more dusty galaxies can provide a more comprehensive understanding of the color gradient establishment. Second, the physical properties of the galaxy including SFR, dust attenuation, and AGN activity can be derived using broadband SED fitting, which can provide a more comprehensive understanding of the origin of color gradient. Third, though we have ruled out the possibility that AGN is the main driver for the excess of positive color gradient in our sample, we are still not sure how much the presence of AGN can influence the color structure of host galaxies at high- z . This could be further examined and confirmed with more spectral information in the future.

- 1 LCH was supported by the National Key R&D Pro-
- 2 gram of China (2022YFF0503401), the National Sci-
- 3 ence Foundation of China (11991052, 12233001), and
- 4 the China Manned Space Project (CMS-CSST-2021-
- 5 A04, CMS-CSST-2021-A06). We thank Chang-Hao
- 6 Chen, Fangzhou Jiang, Limin Lai, Ruancun Li, Yang Li,
- 7 Zhaoyu Li, Chao Ma, Jinyi Shangguanm and Ming-Yang
- 8 Zhuang for valuable discussions and technical support.

Facilities: JWST (NIRCam)

Software: **Astropy** (The Astropy Collaboration et al. 2013), **Galfit** (Peng et al. 2002; Peng et al. 2010), **GalfitM** (Häußler et al. 2013; Vika et al. 2013), **eazy-py** (Brammer et al. 2008), **Photutils** (Bradley et al. 2024), **Matplotlib** (Hunter 2007), **NumPy** (Harris et al. 2020), **SciPy** (Virtanen et al. 2020)

APPENDIX

A. COLOR GRADIENT ANALYSIS

Table A1 presents the catalog of parameters derived from the color gradient analysis.

Table A1. Multi-wavelength Structural Parameter Catalog Entries

Column	Format	Name	Description
1	STRING	Name	Object name from Stefanon et al. (2017)
2	DOUBLE	RAdeg	Right ascension in decimal degrees (J2000.0)
3	DOUBLE	Decdeg	Declination in decimal degrees (J2000.0)
4	DOUBLE	z	Redshift
5	DOUBLE	logMs	Stellar mass from Stefanon et al. (2017)
6	DOUBLE	e_logMs	Mean error on $\log M_*$
7	DOUBLE	F150WRe	The measurement of half-light radius R_e in F150W
8	DOUBLE	e_F150WRe	Mean error on R_e in F150W
9	DOUBLE	F150Wn	The measurement of Sérsic index n in F150W
10	DOUBLE	e_F150WRe	Mean error on n in F150W
11	DOUBLE	F444WRe	The measurement of half-light radius R_e in F444W
12	DOUBLE	e_F444WRe	Mean error on R_e in F444W
13	DOUBLE	F444Wn	The measurement of Sérsic index n in F444W
14	DOUBLE	e_F444Wn	Mean error on n in F444W
15	DOUBLE	q	The measurement of axis ratio q
16	DOUBLE	e_q	Mean error on q
17	DOUBLE	PA	The measurement of position angle PA
18	DOUBLE	e_PA	Mean error on PA
19	STRING	RestFrameOpticalBand	The rest-frame optical band
20	DOUBLE	ReOpt	The measurement of half-light radius R_e in the rest-frame optical band
21	DOUBLE	e_ReOpt	Mean error on ReOpt
22	DOUBLE	nOpt	The measurement of Sérsic index n in the rest-frame optical band
23	DOUBLE	e_nOpt	Mean error on nOpt
24	DOUBLE	Umag	Magnitude (apparent) in rest-frame U from eazy-py
25	DOUBLE	e_Umag	Mean error on Umag
26	DOUBLE	Vmag	Magnitude (apparent) in rest-frame V from eazy-py
27	DOUBLE	e_Vmag	Mean error on Vmag
28	DOUBLE	Jmag	Magnitude (apparent) in rest-frame J from eazy-py
29	DOUBLE	e_Jmag	Mean error on Jmag
30	DOUBLE	ChisqGalfitM	The reduced chi-square from GalfitM
31	LONG	FlagBLD	The blendness flag
32	DOUBLE	F115Wfnu	The measurement of flux in F115W
33	DOUBLE	e_F115Wfnu	Mean error on flux in F115W
34	DOUBLE	F150Wfnu	The measurement of flux in F150W
35	DOUBLE	e_F150Wfnu	Mean error on flux in F150W
36	DOUBLE	F200Wfnu	The measurement of flux in F200W
37	DOUBLE	e_F200Wfnu	Mean error on flux in F200W
38	DOUBLE	F277Wfnu	The measurement of flux in F277W
39	DOUBLE	e_F277Wfnu	Mean error on flux in F277W
40	DOUBLE	F356Wfnu	The measurement of flux in F356W
41	DOUBLE	e_F356Wfnu	Mean error on flux in F356W
42	DOUBLE	F410Mfnu	The measurement of flux in F410M
43	DOUBLE	e_F410Mfnu	Mean error on flux in F410M
44	DOUBLE	F444Wfnu	The measurement of flux in F444W
45	DOUBLE	e_F444Wfnu	Mean error on flux in F444W

Continued on Next Page...

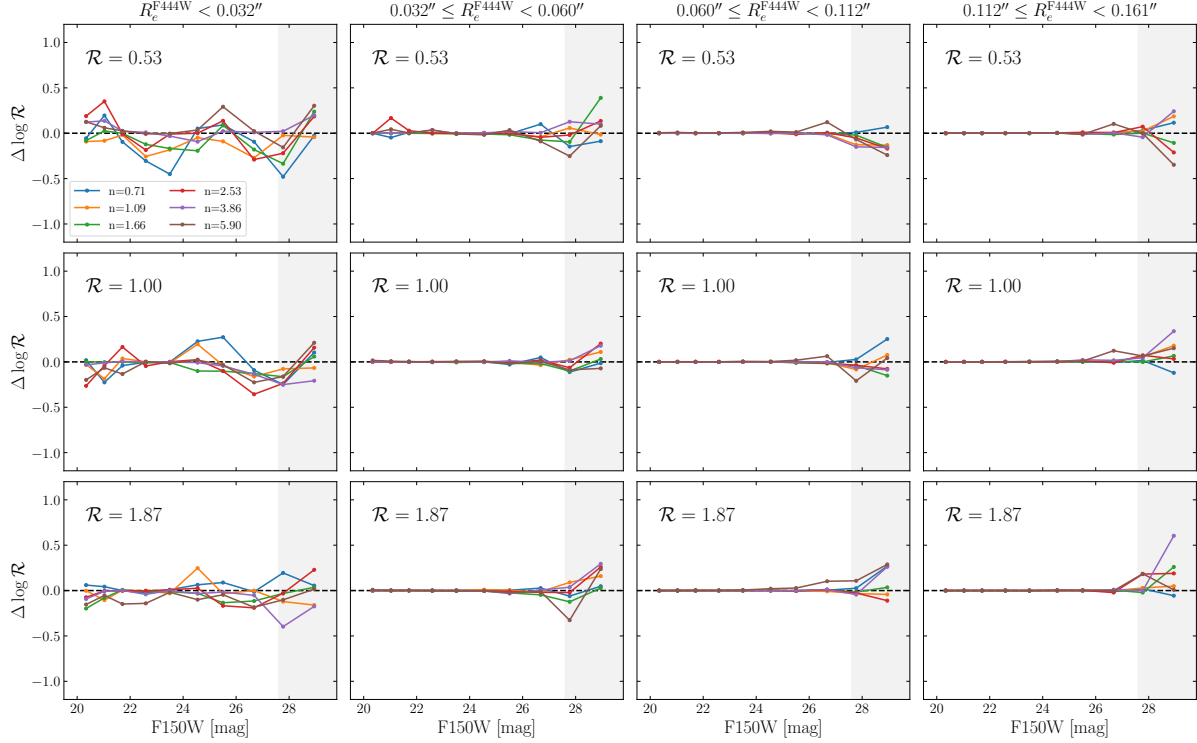


Figure B1. The bias of \mathcal{R} as a function of magnitude in F150W, for $\mathcal{R} = 0.53$ (top), 1.00 (middle), and 1.87 (bottom), and, for columns from left to right, different values in input R_e^{F444W} . The colors indicate the input values of the Sérsic index n at F444W. The grey shaded region marks the magnitude range below 5σ detection at HST/WFC3 F160W.

Table A1 – Continued

Column	Format	Name	Description
46	LONG	FlagHOST	The potential AGN-host galaxy flag

B. MOCK TEST OF COLOR GRADIENT PROXIES

We present a simple illustration of the mock analysis described in Section 3.2, by displaying some typical scenarios. These scenarios span a wide range of parameter space, which covers our sample space well. The bias is the difference between the input and the output parameter values.

For the variation of the effective radius (\mathcal{R}), based on our measurement, we choose to use $\mathcal{R} = 0.53, 1.00$, and 1.87 as representative of the parameter space. In Figure B1, we find that for the latter 3 size bins (column 2, 3, and 4), the measurement is stable and accurate. This indicates that \mathcal{R} can be well measured at approximately $R_e > 0''.4$. If we look into each panel, we can see all measurements become unreliable at the faintest end (> 28 mag).

Similarly, we use $\mathcal{N} = 0.53, 1.00, 1.87$ as representatives of the parameter space. From Figure B2, the measurement of \mathcal{N} is no longer accurate in column 2, so it propels us to make a stricter size cut ($R_e \approx 0''.6$). The trend with the observed magnitude can still be seen, which indicates a magnitude cut here (> 28 mag).

As for $\nabla_{F150W-F444W}$, from Figure B3, the measurement in columns 3 and 4 can still be secure. Overall, a size cut of $R_e \approx 0''.6$ should be enough for all 3 color gradient indicators. We also need a magnitude cut (~ 28 mag) for $\nabla_{F150W-F444W}$. We confirm that the criteria we apply are enough to assure the precision of the measurements across different filters, by studying typical scenarios shown in Figure B1-B3 in different filters.

C. ROBUSTNESS CHECK OF THE SIZE DEPENDENCE

We conduct a robustness check by comparing the statistics derived using the effective radius measured in different bands as the size proxy. We show the comparison in Figure C1, where the trend is consistent with the result derived

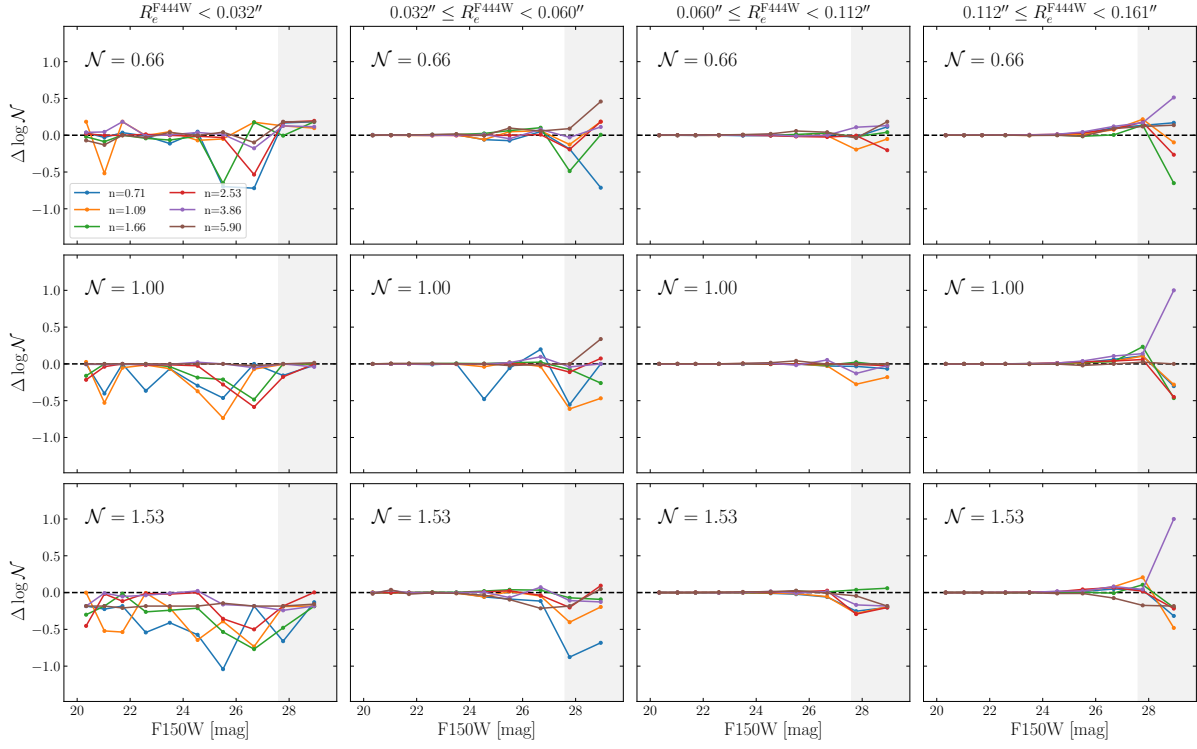


Figure B2. As in Figure B1, but for the bias of \mathcal{N} , for $\mathcal{N} = 0.66$ (top), 1.00 (middle), and 1.53 (bottom).

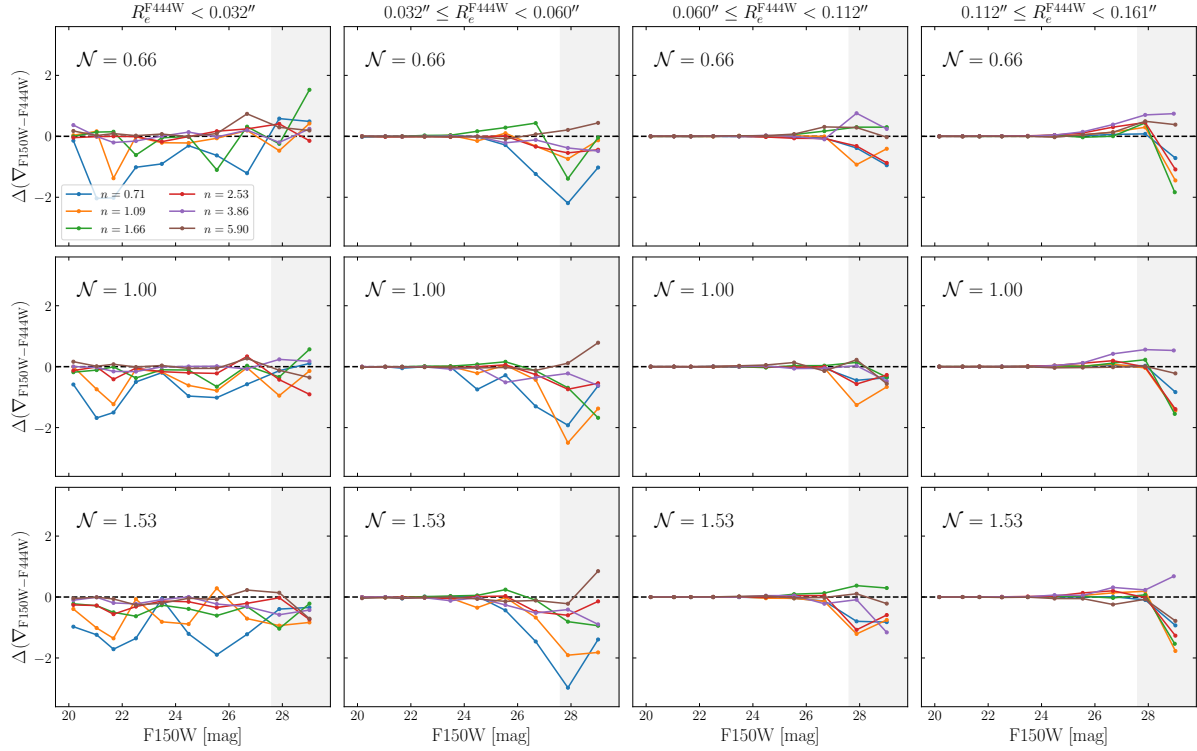


Figure B3. As in Figure B1, but for the bias of $\nabla_{F150W-F444W}$, for $\mathcal{N} = 0.66$ (top), 1.00 (middle), and 1.53 (bottom).

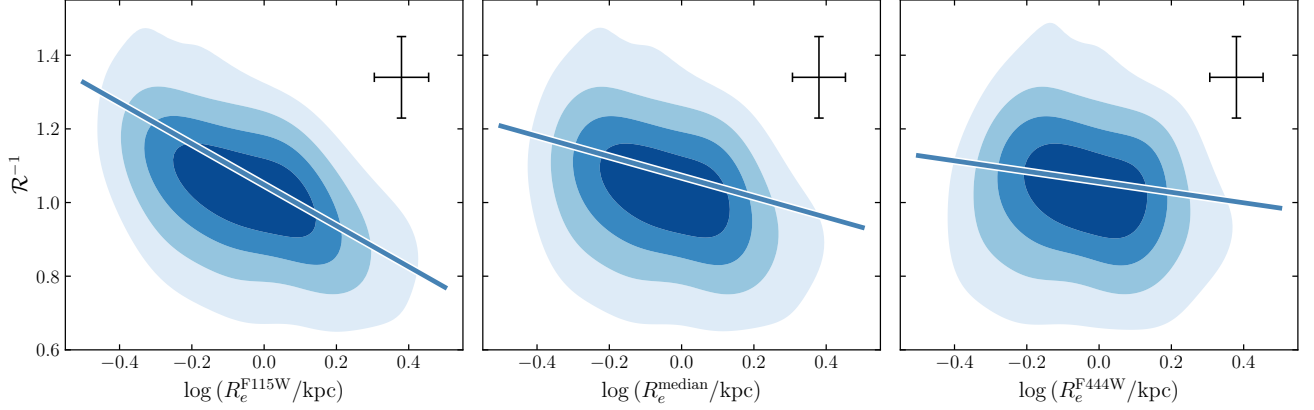


Figure C1. Dependence of the variation in effective radius \mathcal{R} on galaxy effective radius R_e measured in F115W (left), as the median of different bands (middle), and in F444W (right). The solid line gives the best-fit linear regression. The error bars indicate the median uncertainty of the data points. The blue-filled contour shows the density distribution of the data points, where darker color signifies higher density.

using rest-frame optical size, with a diminishing slope as the band moves towards a longer wavelength. In fact, the trend of the diminishing slope with wavelength does not have extra physical implications. It is the mathematical result of the correlation between \mathcal{R} and galaxy sizes. Even in the right panel of Figure C1, the increasing trend is still perceivable.

REFERENCES

- Abdurro'uf, & Akiyama, M. 2018, MNRAS, 479, 5083
- Abdurro'uf, Coe, D., Jung, I., et al. 2023, ApJ, 945, 117
- Akins, H. B., Casey, C. M., Berg, D. A., et al. 2024, ApJL, submitted (arXiv:2410.00949)
- Baggen, J. F. W., van Dokkum, P., Brammer, G., et al. 2024, ApJL, submitted (arXiv:2408.07745)
- Bagley, M. B., Finkelstein, S. L., Koekemoer, A. M., et al. 2023a, ApJL, 946, L12
- Bagley, M. B., Pirzkal, N., Finkelstein, S. L., et al. 2024, ApJL, 965, L6
- Baker, W. M., Tacchella, S., Johnson, B. D., et al. 2024, Nature Astronomy, submitted (arXiv:2306.02472)
- Bradley, L., Sipőcz, B., Robitaille, T., et al. 2024, Astropy/Photutils: 1.12.0, Zenodo
- Brammer, G. B., van Dokkum, P. G., & Coppi, P. 2008, ApJ, 686, 1503
- Calzetti, D., Armus, L., Bohlin, R. C., et al. 2000, ApJ, 533, 682
- Cappellari, M., McDermid, R. M., Alatalo, K., et al. 2013, MNRAS, 432, 1862
- Casey, C. M., Kartaltepe, J. S., Drakos, N. E., et al. 2023, ApJ, 954, 31
- Ceverino, D., Klypin, A., Klimek, E. S., et al. 2014, MNRAS, 442, 1545
- Cheng, C., Xu, C. K., Xie, L., et al. 2020, A&A, 633, A105
- Dekel, A., Ginzburg, O., Jiang, F., et al. 2020, MNRAS, 493, 4126
- Driver, S. P., Andrews, S. K., da Cunha, E., et al. 2018, MNRAS, 475, 2891
- Duncan, K., Conselice, C. J., Mundy, C., et al. 2019, ApJ, 876, 110
- Eggen, O. J., Lynden-Bell, D., & Sandage, A. R. 1962, ApJ, 136, 748

- Eisenstein, D. J., Willott, C., Alberts, S., et al. 2024, *ApJS*, submitted (arXiv:2306.02465)
- Finkelstein, S. L., Bagley, M. B., Ferguson, H. C., et al. 2023, *ApJL*, 946, L13
- Forbes, D. A., & Bridges, T. 2010, *MNRAS*, 404, 1203
- Frankel, N., Sanders, J., Rix, H.-W., Ting, Y.-S., & Ness, M. 2019, *ApJ*, 884, 99
- Fudamoto, Y., Oesch, P. A., Faisst, A., et al. 2020, *A&A*, 643, A4
- Giménez-Arteaga, C., Oesch, P. A., Brammer, G. B., et al. 2023, *ApJ*, 948, 126
- Gong, J.-Y., Mao, Y.-W., Gao, H., & Yu, S.-Y. 2023, *ApJS*, 267, 26
- Graham, A. W., & Worley, C. C. 2008, *MNRAS*, 388, 1708
- Harikane, Y., Inoue, A. K., Ellis, R. S., et al. 2024, *ApJ*, submitted (arXiv:2406.18352)
- Harikane, Y., Zhang, Y., Nakajima, K., et al. 2023, *ApJ*, 959, 39
- Harris, C. R., Millman, K. J., van der Walt, S. J., et al. 2020, *Nature*, 585, 357
- Harvey, T., Conselice, C., Adams, N. J., et al. 2024, *ApJ*, submitted (arXiv:2403.03908)
- Hasheminia, M., Mosleh, M., Zahra Hosseini-ShahiSavandi, S., et al. 2024, *ApJ*, in press (arXiv:2410.05867)
- Häußler, B., Bamford, S. P., Vika, M., et al. 2013, *MNRAS*, 430, 330
- Häußler, B., Vika, M., Bamford, S. P., et al. 2022, *A&A*, 664, A92
- Ho, L. C., Li, Z.-Y., Barth, A. J., Seigar, M. S., & Peng, C. Y. 2011, *ApJS*, 197, 21
- Hopkins, P. F., Bundy, K., Hernquist, L., et al. 2010, *MNRAS*, 401, 1099
- Huang, S., Ho, L. C., Peng, C. Y., Li, Z.-Y., & Barth, A. J. 2013, *ApJ*, 766, 47
- Hunter, J. D. 2007, *Computing in Science & Engineering*, 9, 90
- Ji, Z., Williams, C. C., Suess, K. A., et al. 2024, *ApJ*, submitted (arXiv:2401.00934)
- Kelvin, L. S., Driver, S. P., Robotham, A. S. G., et al. 2012, *MNRAS*, 421, 1007
- Kennedy, R., Bamford, S. P., Baldry, I., et al. 2015, *MNRAS*, 454, 806
- Kodra, D., Andrews, B. H., Newman, J. A., et al. 2023, *ApJ*, 942, 36
- Koekemoer, A. M., Faber, S. M., Ferguson, H. C., et al. 2011, *ApJS*, 197, 36,
- Kokorev, V., Caputi, K. I., Greene, J. E., et al. 2024, *ApJ*, 968, 38
- Kormendy, J., Drory, N., Bender, R., et al. 2010, *ApJ*, 723, 54
- Kron, R. G. 1980, *ApJS*, 43, 305
- Labbé, I., Greene, J. E., Bezanson, R., et al. 2024, *ApJ*, submitted (arXiv:2306.07320)
- Lapiner, S., Dekel, A., Freundlich, J., et al. 2023, *MNRAS*, 522, 4515
- Larson, R. L., Hutchison, T. A., Bagley, M., et al. 2023, *ApJ*, 958, 141
- Li, Q., Narayanan, D., & Davé, R. 2019, *MNRAS*, 490, 1425
- Li, Z., Inayoshi, K., Chen, K., et al. 2024, *ApJ*, submitted (arXiv:2407.10760)
- Looser, T. J., D'Eugenio, F., Maiolino, R., et al. 2024, *A&A*, submitted (arXiv:2306.02470)
- Lyu, Y., Magnelli, B., Elbaz, D., et al. 2024, *A&A*, submitted (arXiv:2406.11571)
- Magnelli, B., Gómez-Guijarro, C., Elbaz, D., et al. 2023, *A&A*, 678, A83
- Mannering, E. J. A., Worrall, D. M., & Birkinshaw, M. 2011, *MNRAS*, 416, 2869
- Marian, V., Ziegler, B., Kuchner, U., & Verdugo, M. 2018, *A&A*, 617, A34
- Martorano, M., van der Wel, A., Bell, E. F., et al. 2023, *ApJ*, 957, 46
- Matharu, J., Muzzin, A., Sarrouh, G., et al. 2023, *ApJL*, 949, L11
- Matthee, J., Naidu, R. P., Brammer, G., et al. 2024, *ApJ*, 963, 129
- Matharu, J., Nelson, E. J., Brammer, G., et al. 2024, *A&A*, submitted (arXiv:2404.17629)
- Miller, T. B., van Dokkum, P., & Mowla, L. 2023, *ApJ*, 945, 155
- Miller, T. B., Whitaker, K. E., Nelson, E. J., et al. 2022, *ApJL*, 941, L37
- Mitsuhashi, I., Tadaki, K.-i., Ikeda, R., et al. 2024, *A&A*, submitted (arXiv:2311.17671)
- Mo, H. J., Mao, S., & White, S. D. M. 1998, *MNRAS*, 295, 319
- Morishita, T., Stiavelli, M., Chary, R.-R., et al. 2024, *ApJ*, 963, 9
- Mosleh, M., Williams, R. J., Franx, M., et al. 2012, *ApJ*, 756, L12
- Muñoz-Mateos, J. C., Gil de Paz, A., Boissier, S., et al. 2007, *ApJ*, 658, 1006
- Nedkova, K. V., Häußler, B., Marchesini, D., et al. 2024a, *MNRAS*, submitted (arXiv:2406.14613)
- Nedkova, K. V., Rafelski, M., Teplitz, H. I., et al. 2024b, *ApJ*, submitted (arXiv:2405.10908)
- Nelson, E. J., Tacchella, S., Diemer, B., et al. 2021, *MNRAS*, 508, 219
- Nelson, E. J., van Dokkum, P. G., Förster Schreiber, N. M., et al. 2016, *ApJ*, 828, 27

- Ono, Y., Harikane, Y., Ouchi, M., et al. 2024, PASJ, 76, 219
- Overzier, R. A., Heckman, T. M., Schiminovich, D., et al. 2010, ApJ, 710, 979
- Pandya, V., Zhang, H., Huertas-Company, M., et al. 2024, ApJ, 963, 54
- Peng, C. Y., Ho, L. C., Impey, C. D., & Rix, H.-W. 2002, AJ, 124, 266
- Peng, C. Y., Ho, L. C., Impey, C. D., & Rix, H.-W. 2010, AJ, 139, 2097
- Pérez, E., Cid Fernandes, R., González Delgado, R. M., et al. 2013, ApJ, 764, L1
- Pezzulli, G., Fraternali, F., & Binney, J. 2017, MNRAS, stx029
- Planck Collaboration, Aghanim, N., Akrami, Y., et al. 2020, A&A, 641, A6
- Rigby, J., Perrin, M., McElwain, M., et al. 2023, PASP, 135, 048001
- Ryder, S. D., & Dopita, M. A. 1994, ApJ, 430, 142
- Salim, S., & Narayanan, D. 2020, ARA&A, 58, 529
- Sérsic, J. L. 1968, Atlas de Galaxias Australes (Córdoba: Obs. Astron., Univ. Nac. Córdoba)
- Shen, S., Mo, H. J., White, S. D. M., et al. 2003, MNRAS, 343, 978
- Shibuya, T., Ouchi, M., & Harikane, Y. 2015, ApJS, 219, 15
- Skelton, R. E., Whitaker, K. E., Momcheva, I. G., et al. 2014, ApJS, 214, 24
- Stark, D. V., Tuttle, S., Tonnesen, S., et al. 2024, ApJ, in press (arXiv:2406.00635)
- Stefanon, M., Yan, H., Mobasher, B., et al. 2017, ApJS, 229, 32
- Steinmetz, M. & Navarro, J. F. 2002, NewA, 7, 155
- Suess, K. A., Kriek, M., Price, S. H., & Barro, G. 2019, ApJ, 877, 103
- Sun, G., Faucher-Giguère, C.-A., Hayward, C. C., et al. 2023, ApJL, 955, L35
- Sun, W., Ho, L. C., Zhuang, M.-Y., et al. 2024, ApJ, 960, 104
- Tacchella, S., Carollo, C. M., Förster Schreiber, N. M., et al. 2018, ApJ, 859, 56
- Tacchella, S., Carollo, C. M., Renzini, A., et al. 2015, Science, 348, 314
- Tacchella, S., Dekel, A., Carollo, C. M., et al. 2016, MNRAS, 457, 2790
- Tacchella, S., Forbes, J. C., & Caplar, N. 2020, MNRAS, 497, 698
- Taylor, A. J., Finkelstein, S. L., Kocevski, D. D., et al. 2024, ApJ, submitted (arXiv:2409.06772)
- The Astropy Collaboration, Robitaille, T. P., Tollerud, E. J., et al. 2013, A&A, 558, A33
- Tomassetti, M., Dekel, A., Mandelker, N., et al. 2016, MNRAS, 458, 4477
- Tonnesen, S., DeFelippis, D., & Tuttle, S. 2023, ApJ, 951, 16
- Treu, T., Calabro, A., Castellano, M., et al. 2023, ApJL, 942, L28
- Tripodi, R., D'Eugenio, F., Maiolino, R., et al. 2024, A&A, submitted (arXiv:2403.08431)
- Tuttle, S. E. & Tonnesen, S. 2020, ApJ, 889, 188
- Vader, J. P., Vigroux, L., Lachieze-Rey, M., & Souviron, J. 1988, A&A, 203, 217
- van der Wel, A., Chang, Y.-Y., Bell, E. F., et al. 2014a, ApJL, 792, L6
- van der Wel, A., Franx, M., van Dokkum, P. G., et al. 2014b, ApJ, 788, 28
- van der Wel, A., Martorano, M., Häußler, B., et al. 2024, ApJ, 960, 53
- van Dokkum, P. G., Leja, J., Nelson, E. J., et al. 2013, ApJL, 771, L35
- van Dokkum, P. G., Whitaker, K. E., Brammer, G., et al. 2010, ApJ, 709, 1018
- Vika, M., Bamford, S. P., Haeussler, B., et al. 2013, MNRAS, 435, 623
- Vika, M., Vulcani, B., Bamford, S. P., Häußler, B., & Rojas, A. L. 2015, A&A, 577, A97
- Virtanen, P., Gommers, R., Oliphant, T. E., et al. 2020, Nature Methods, 17, 261
- Vulcani, B., Bamford, S. P., Häußler, B., et al. 2014, MNRAS, 441, 1340
- Wang, B., Leja, J., Labbé, I., et al. 2024, ApJS, 270, 12
- Wang, J., Navarro, J. F., Frenk, C. S., et al. 2011, MNRAS, 413, 1373
- Wang, W., Faber, S. M., Liu, F. S., et al. 2017, MNRAS, 469, 4063
- Ward, E. M., de la Vega, A., Mobasher, B., et al. 2024, ApJ, 962, 176
- White, S. D. M., & Frenk, C. S. 1991, ApJ, 379, 52
- Whitney, A., Ferreira, L., Conselice, C. J., & Duncan, K. 2021, ApJ, 919, 139
- Williams, R. J., Quadri, R. F., Franx, M., van Dokkum, P., & Labbé, I. 2009, ApJ, 691, 1879
- Yang, L., Morishita, T., Leethochawalit, N., et al. 2022, ApJL, 938, L17
- York, D. G., Adelman, J., Anderson, J. E., et al. 2000, AJ, 120, 1579
- Zhang, H., Primack, J. R., Faber, S. M., et al. 2019, MNRAS, 484, 5170
- Zhang, J., Wuyts, S., Cutler, S. E., et al. 2023, MNRAS, 524, 4128
- Zhuang, M.-Y., & Ho, L. C. 2022, ApJ, 934, 130

Zhuang, M.-Y., Li, J., & Shen, Y. 2024, ApJ, 962, 93
Zhuang, M.-Y., & Shen, Y. 2024, ApJ, 962, 139

Zolotov, A., Dekel, A., Mandelker, N., et al. 2015, MNRAS,
450, 2327